



저작자표시-비영리-변경금지 2.0 대한민국

이용자는 아래의 조건을 따르는 경우에 한하여 자유롭게

- 이 저작물을 복제, 배포, 전송, 전시, 공연 및 방송할 수 있습니다.

다음과 같은 조건을 따라야 합니다:



저작자표시. 귀하는 원저작자를 표시하여야 합니다.



비영리. 귀하는 이 저작물을 영리 목적으로 이용할 수 없습니다.



변경금지. 귀하는 이 저작물을 개작, 변형 또는 가공할 수 없습니다.

- 귀하는, 이 저작물의 재이용이나 배포의 경우, 이 저작물에 적용된 이용허락조건을 명확하게 나타내어야 합니다.
- 저작권자로부터 별도의 허가를 받으면 이러한 조건들은 적용되지 않습니다.

저작권법에 따른 이용자의 권리는 위의 내용에 의하여 영향을 받지 않습니다.

이것은 [이용허락규약\(Legal Code\)](#)을 이해하기 쉽게 요약한 것입니다.

[Disclaimer](#)

공학박사 학위논문

Effect of Substrate Bias on Deposition
Behavior of Charged Silicon Nanoparticles in
ICP-CVD Process

유도결합플라즈마를 이용한
화학기상증착 공정 중에 생성되는
하전된 실리콘 나노 입자의 증착
거동에 대한 기판 바이어스 효과

2016 년 8 월

서울대학교 대학원

재료공학부

유 승 완

Effect of Substrate Bias on Deposition Behavior of Charged Silicon Nanoparticles in ICP-CVD Process

지도교수 황 농 문

이 논문을 공학박사 학위논문으로 제출함

2016 년 7 월

서울대학교 대학원

재료공학부

유 승 완

유승완의 공학박사 학위논문을 인준함

2016 년 7 월

위 원 장

이 정 중

(인)

부위원장

황 농 문

(인)

위 원

김 미 영

(인)

위 원

정 용 빈

(인)

위 원

홍 주 섭

(인)

Abstract

Effect of Substrate Bias on Deposition Behavior of Charged Silicon Nanoparticles in ICP-CVD Process

Seung-Wan Yoo

Department of Materials Science and Engineering

The Graduate School

Seoul National University

The effect of a substrate bias on the deposition behavior of crystalline silicon nanoparticles during inductively coupled plasma chemical vapor deposition (ICP-CVD) was approached by nonclassical crystallization, in which the building block is a nanoparticle rather than an individual atom or molecule. This study consists of two major parts. One is the effect of the substrate bias on the deposition behavior of crystalline silicon nanoparticles during the thin-film deposition condition in the ICP-CVD process. The other is the effect of the substrate bias on the deposition behavior of crystalline silicon nanoparticles during the nanoparticle synthesis condition in the ICP-CVD process

In the first part, the coexistence of positively and negatively charged nanoparticles in the plasma and their role in Si film deposition are confirmed by applying a bias voltage on the substrate, which is so small as not to vary the plasma potential. The sizes of positively and negatively charged nanoparticles captured on the TEM grid membrane were respectively 2.7 ~ 5.5 nm and 6 ~ 13 nm. The film deposited by positively charged nanoparticles has a typical columnar structure. In contrast, the film deposited by negatively charged nanoparticles has the structure like a powder compact with the deposition rate about three times higher than that deposited by positively charged nanoparticles. All the films have crystallinity although the substrate is at room temperature, which is attributed to the deposition of crystalline nanoparticles formed in the plasma. The film deposited by negatively charged nanoparticles has the highest crystalline fraction of 0.84.

In the second part, the effect of the substrate bias on the size and amount of crystalline silicon nanoparticles deposited on the substrate with inserting grounded grids are investigated in an inductively coupled plasma chemical vapor deposition (ICP-CVD) process. By inserting grounded grids above the substrate, the lower region of the grounded grids was separated from the plasma. Thereby, the film formation in the ICP-CVD process could be avoided on the substrate and as a result crystalline Si nanoparticles formed in the plasma could be deposited on the substrate. Moreover the size and the amount of nanoparticles could be controlled by applying the direct current (DC) bias on the substrate. When the 1 mm square mesh grid was used, the nanoparticle flux was increased as the negative substrate bias was increased from 0 V to - 50 V. On the other hand, when positive biases were applied to the substrate, Si nanoparticles were not deposited at all. When the 2

mm square mesh grid was used, sizes of nanoparticles were increased as the substrate bias was increased from -50 V to 50 V.

Keywords: silicon thin film, charged nanoparticles, nonclassical crystallization, ICP-CVD, substrate bias

Student Number: 2009-20620

Contents

1. Introduction

1.1. Theory of Charged Nanoparticles -----	1
1.1.1 Introduction to Non-classical crystallization-----	1
1.1.2 Charged Nanoparticles in Diamond CVD-----	3

2. Effect of Substrate Bias on Deposition Behavior of Charged Silicon Nanoparticle in ICP-CVD Process

2.1 Introduction -----	9
2.2 Experiments -----	12
2.3 Results and Discussion -----	15
2.4 Conclusions -----	26

3. Application of Charged Nanoparticles Theory in ICP-CVD

**process: Enhancement of Generation of Positively Charged
Nanoparticles**

3.1 Introduction -----	28
3.2 Experiments -----	29
3.3 Results and Discussion -----	31
3.4 Conclusions -----	36

**4. Control of Nanoparticle Size and Their Amount by Using
the Mesh Grid and the DC-Biased Substrate in Silane ICP-
CVD Process**

4.1 Introduction -----	37
4.2 Experiments -----	38
4.3 Results and Discussion -----	40
4.4 Conclusions -----	55

List of figures

Figure 1. Thermodynamic and kinetic description of the metastable diamond formation-----3

Figure 2. Dependence of Gibbs free energy on the number of atoms for diamond and graphite. The dashed and long-dashed lines are for diamond respectively with 10% and 20% reduction of the surface energy-----4

Figure 3. Comparison of chemical potential of carbon for graphite, diamond, and gas based on (a) phase diagram of carbon and (b) atomic hydrogen hypothesis-----5

Figure 4. Comparison of chemical potential of carbon between diamond, graphite, gas, and gas phase nuclei with the direction of their flux-----6

Figure 5. Mass distribution of negatively charged carbon clusters extracted from the HWCVD reactor using 1%CH₄-99%H₂, 1.5%CH₄-98.5%H₂, 3%CH₄-97%H₂, and 5%CH₄-95%H₂ gas mixtures, at a wire temperature of 2100°C under the reactor pressure of 800 Pa-----7

Figure 6. SEM images of diamond films deposited at the same conditions as the figure 5: (a) 1%CH₄-99%H₂, (b) 3%CH₄-97%H₂-----8

Figure 7. Plasma potentials measured with various bias voltages which were applied to a substrate of 20 cm in diameter and a small substrate of $3 \times 5 \text{ mm}^2$ ---13

Figure 8. Cross-sectional FE-SEM images of Si films deposited for 4 min on p-type silicon wafer at substrate biases of (a) -10 V and (b) 40 V-----14

Figure 9. Deposition rates of Si films deposited for 4 min with various substrate biases from -10 V to 40 V-----16

Figure 10. Cross-sectional FE-SEM images of Si films deposited for 4 min on a graphite substrate at substrate biases of (a) -10 V, (b) 10 V, (c) 20 V, (d) 30 V, and (e) 40 V-----20

Figure 11. Raman spectra of Si films deposited at the same condition as in Figure 9. Crystalline volume fractions were estimated as 0.84, 0.59, 0.56, 0.24, and 0.12 at substrate biases of 40, 30, 20, 10, and -10 V, respectively-----22

Figure 12. Cross-sectional TEM images for Si films prepared at substrate biases of (a) 40 V and (c) 10V at the same condition as in Figure 9. Images of (b) and (d) are high-resolution images of (a) and (c), respectively-----24

Figure 13. Plane view high-resolution TEM images of Si nanoparticles captured on the membrane of TEM grids at substrate biases of (a) 40 V and (b) 10 V-----25

Figure 14. Schematic of the experimental setup-----30

Figure 15. Cross-sectional FE-SEM images of Si thin films deposited on graphite for 4 min under the reactor pressure of 350 mTorr with the showerhead of (a) 30, (b) 24, (c) 10, (d) 0 cm in diameter when the substrate bias was -10 V-----32

Figure 16. Raman spectra of Si films deposited at the same condition as in figure 15-----33

Figure 17. Cross-sectional FE-SEM images of Si thin films deposited on graphite for 4 min under the reactor pressure of 350 mTorr with the showerhead of (a) 30, (b) 24, (c) 10, (d) 0 cm in diameter when the substrate bias was 40 V-----35

Figure 18. Schematic of the planar ICP chamber-----39

Figure 19. SEM images of Si Nanoparticles deposited on silicon wafer substrate at V_{sub} of 0 V with grounded grid of (a) 1 mm and (b) 2 mm meshes. High-resolution TEM images of Si nanoparticles deposited on the membrane of TEM grids at V_{sub} of 0 V with grounded grid of (c) 1 mm and (d) 2 mm meshes -----41

Figure 20. Size distributions and number density of Si nanoparticles for substrate bias of (a) -50, (b) -25, (c) 0, (d) 25, and (e) 50 V with grounded grid of 1 mm

meshes at RF power of 1400 W-----43

Figure 21. Microscopic diagrams for one cell of the grid (a) when the sheath is thick enough to overlap the hole of mesh, (b) when the sheath exist with the sheath-free region-----45

Figure 22. Size distributions and number density of Si nanoparticles for substrate bias of (a) -50, (b) -25, (c) 0, (d) 25, and (e) 50 V with grounded grid of 2 mm meshes at RF power of 1400 W-----46

Figure 23. Plasma potentials measured with substrate bias of -50, 0, and 50 V at RF power of 1400 W for grounded grid of 1 mm and 2 mm meshes-----47

Figure 24. SEM images of Si Nanoparticles deposited by RF power of 1000 W at substrate bias of (a) -50, (b) 0, and (c) 50 V with grounded grid of 2 mm meshes-----50

Figure 25. Size distributions and number density of Si nanoparticles for substrate bias of (a) -50, (b) 0, and (c) 50 V with grounded grid of 2 mm meshes at RF power of 1700 W-----51

Figure 26. Microscopic diagrams for one cell of the grid (a) when the sheath exists with the sheath-free region, (b) when the sheath is too thin to confine the substrate

from the plasma-----52

Figure 27. Size distributions and number density of Si nanoparticles for substrate bias of (a) -50, (b) 0, and (c) 50 V with grounded grid of 1 mm meshes at RF power of 1700 W-----54

Chapter I. Introduction

1.1. Theory of Charged Nanoparticles

1.1.1 Introduction to Non-classical crystallization

Crystal is a structure where atoms consists a lattice regularly. Classically, it is considered that the building block of crystal is an individual atom or a molecule and this concept is called classical crystallization. In classical crystallization, the crystal growth is described by the terrace, ledge and kink (TLK) model. In this model, atoms first land on the terrace, diffuse to the ledge and finally become incorporated into a crystal at the kink.[1, 2].

However, there have been many evidences indicating that the building block of crystal growth is an individual nanoparticle, and this new concept about crystallization is called non-classical crystallization. Cölfen and Antonietti [3] made an extensive review on non-classical crystallization and made a meaningful remark that reanalyzing the literature, this mechanism turns out to be a “rediscovery”, as it seems that many important original observations are meanwhile forgotten and hidden in the past literature, as they simply did not comply with the classical crystallization model. A concept similar to non-classical crystallization was already suggested by Glasner et al.[4-7] during their study of the crystal growth of KBr and KCl in the presence of Pb^{2+} in aqueous solution. At the time, their suggestion was so revolutionary as to receive severe criticism,[8] and was subsequently dismissed by the crystal growth community. Sunagawa[9, 10]

made a similar suggestion that the growth unit of synthetic diamond is not an atom but a much larger unit, which has not been taken seriously in the community of diamond synthesis.

A similar concept has been more recently suggested in the plasma-enhanced chemical vapor deposition (CVD) process by Cabarrocas,[11, 12] Vladimirov and Ostrikov,[13] and Nunomura et al. [14] In this process, the incorporation of crystalline Si nanoparticles into the films produces a so-called polymorphous structure.[9, 10]

Hwang et al. reported that diamonds synthesized at low pressure by chemical vapor deposition (CVD) grow by nanoparticles formed in the gas phase.[15-17] This was extensive study about the non-classical crystallization of CVD diamonds. Since then Hwang et al.[15, 17-29] demonstrated that electrically charged nanoparticles play a critical role in the evolution of dense films, whereas neutral nanoparticles produce porous aggregations.[30] The generation of charged nanoparticles (CNPs), which was predicted to form in the gas phase during CVD was experimentally confirmed in many CVD process. [19, 25-29, 31-33]

1.1.2 Charged Nanoparticles in Diamond CVD

Diamond synthesis in high-temperature and high-pressure process is considered as thermodynamically stable process because the phase diagram of carbon justifies the diamond synthesis in high-temperature and high-pressure process. However the low-pressure synthesis of diamond cannot be understood because diamond is metastable phase under the low pressure.[34, 35]

Hwang and Lee explained the formation of metastable diamond can be possible in low pressure synthesis. Although graphite is more stable than diamond at low pressure, diamond is more stable than gas as shown in figure 1. Therefore, if the kinetic barrier of the formation of the metastable diamond lower than that of the graphite, the formation of the diamond can be possible.

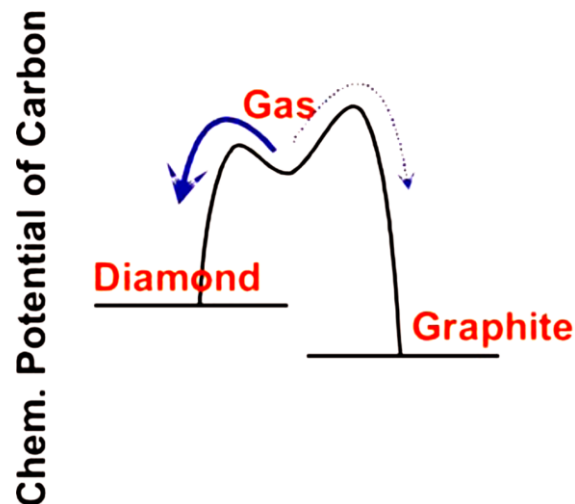


Figure 1. Thermodynamic and kinetic description of the metastable diamond formation.[36]

Figure 2 shows the dependence of Gibbs free energy on the number of atoms for diamond and graphite.[37] The Gibbs free energy of diamond is slightly smaller than that of graphite in the range between 0 and ~ 260 carbon atoms. However, the kinetic barrier of the formation of diamond is still larger than that of graphite because the maxima point of the Gibbs free energy of diamond is larger than that of the Gibbs free energy of graphite, which are correspond to the kinetic barrier of the formation of diamond or graphite respectively. However, if the surface energy is reduced, the nucleation barrier of diamond is lower than that of graphite. Therefore the surface energy reduction of diamond would be one possibility of stabilization of diamond.

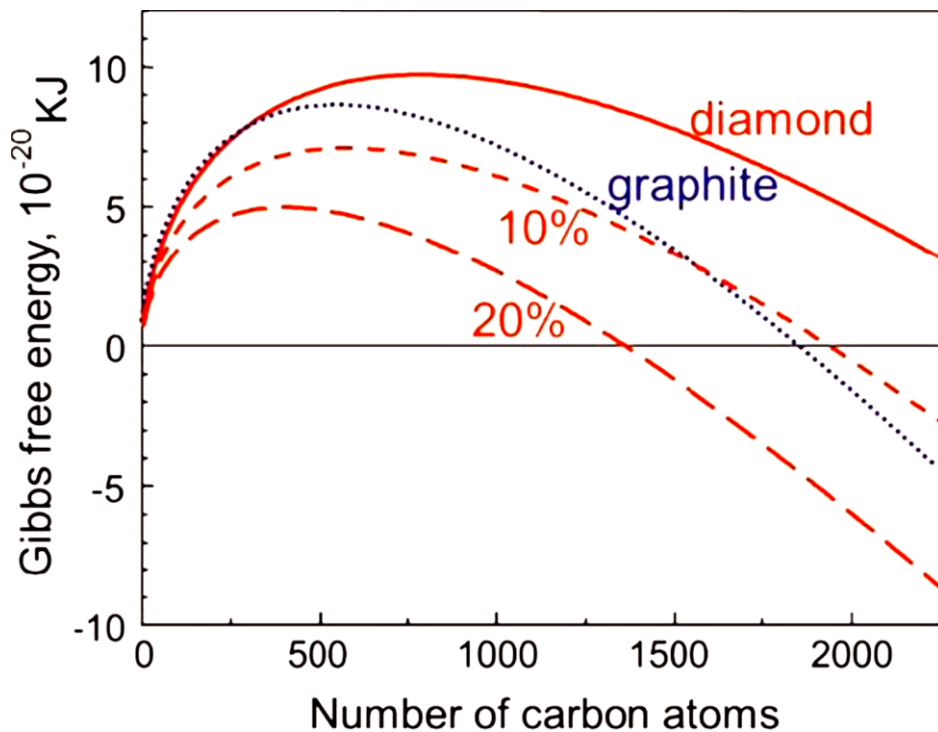


Figure 2. Dependence of Gibbs free energy on the number of atoms for diamond (solid line) and graphite (dotted line). The dashed and long-dashed lines are for

diamond respectively with 10% and 20% reduction of the surface energy.[36]

It was observed experimentally in the 1980s that the diamond was formed dominantly over graphite when gas activation such as hot filament and plasma was used, which was contrary to the fact that graphite was formed dominantly over diamond without gas activation. This was attributed to the production of the atomic hydrogen. The popular theory called as atomic hydrogen hypothesis suggested that the atomic hydrogen, which can be produced by hot filament or plasma, etches graphite much faster than diamond, and make diamond deposited.

However this explanation violates the second law of thermodynamic.[17] As shown in figure 3 (b), atomic hydrogen hypothesis considers that chemical potential of graphite is higher than diamond. However, based on the phase diagram of carbon, chemical potential is graphite is lower than that of diamond.

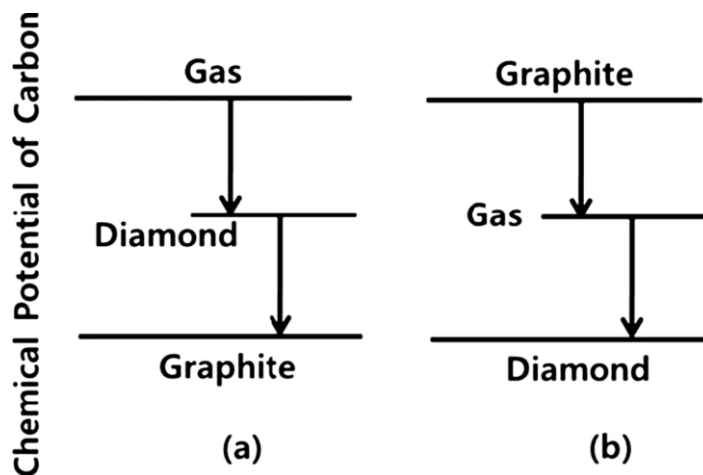


Figure 3. Comparison of chemical potential of carbon for graphite, diamond, and gas based on (a) phase diagram of carbon and (b) atomic hydrogen hypothesis.[36]

Hwang et al. tried to explain the experimental observation that diamond can be deposited under the condition where graphite simultaneously etches into the gas phase. Avoiding the violation of the second law of thermodynamic in explanation of the puzzling experimental observation, Hwang et al. suggested that diamond gas phase nuclei should be the building block of diamond films as illustrated in figure 4.

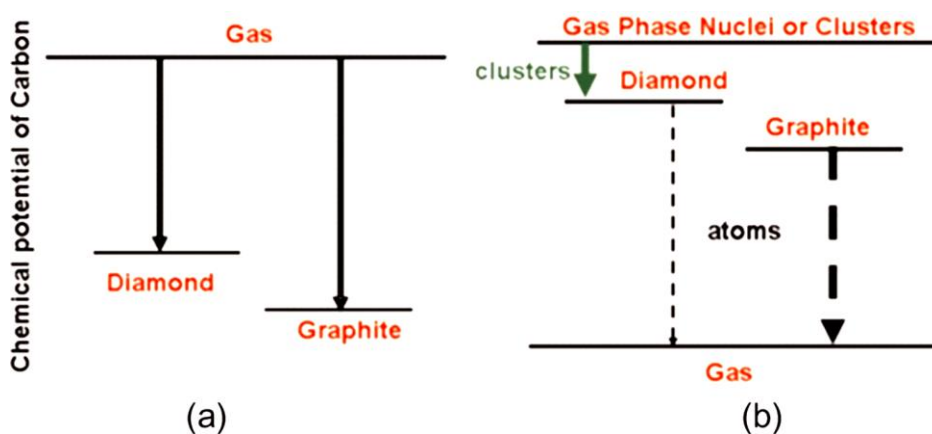


Figure 4. Comparison of chemical potential of carbon between diamond, graphite, gas, and gas phase nuclei with the direction of their flux.

According to the explanation, at the substrate, both the diamond and the graphite are etched, while the diamond nuclei are generated in the gas phase and deposited.

To confirm the generation of diamond gas phase nuclei, Jeon et al.[19, 38] measured the mass distribution of negatively charged nanoparticles of carbon formed in the gas phase with various CH_4 concentrations at a wire temperature of

2100°C under 800 Pa in the hot filament CVD process [39]. And diamonds were also deposited during the measurements of mass distribution as shown in figure 5.

In figure 5, for the condition of 1 % CH₄, the peak occurred at ~ 3000 atomic mass units and high-quality diamonds crystals were observed as shown in figure 6 (a). In contrast, for the condition of 3% CH₄, the mass distribution became much broader than that for 1 % CH₄ and the cauliflower structures were deposited as shown in figure 6 (b). Considering the mass distribution of negatively charged nanoparticles shown in figure 5 and the morphology of nanostructure shown in figure 6, it is concluded that there was correlation between the negatively charged nanoparticles in the gas phase and the nanostructure on the substrate. Therefore, this result implies that the diamond deposited on the substrate grow by charged diamond nanoparticles generated in the gas phase.

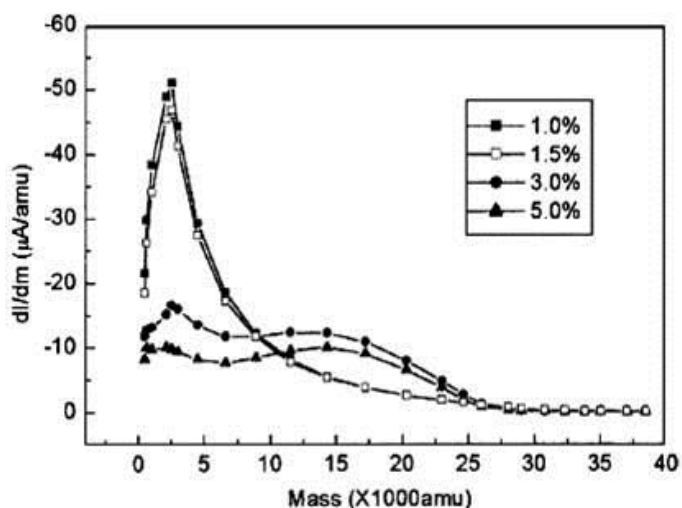


Figure 5. Mass distribution of negatively charged carbon clusters extracted from

the HW-CVD reactor using 1%CH₄-99%H₂, 1.5%CH₄-98.5%H₂, 3%CH₄-97%H₂, and 5%CH₄-95%H₂ gas mixtures, at a wire temperature of 2100°C under the reactor pressure of 800 Pa [39].

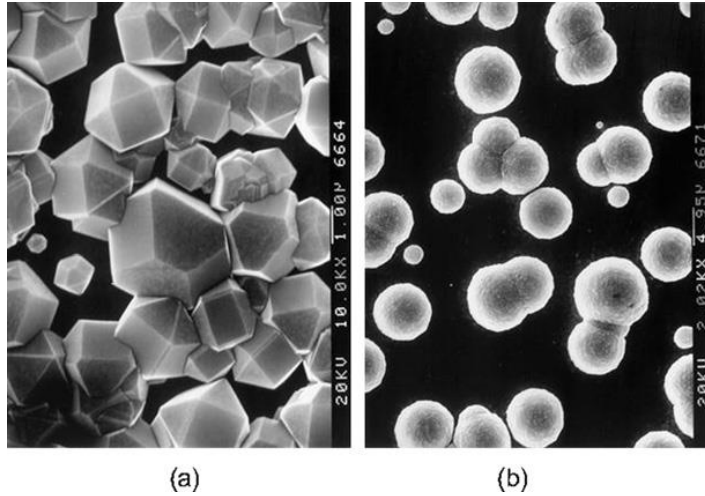


Figure 6. SEM images of diamond films deposited at the same conditions as the figure 5: (a) 1%CH₄-99%H₂, (b) 3%CH₄-97%H₂. [40]

Chapter II. Effect of Substrate Bias on Deposition Behavior of Charged Silicon Nanoparticle in ICP-CVD Process

1. INTRODUCTION

Since early 1990s, non-classical crystallization, where the building block of crystal growth is not an individual atom or molecule but a nanoparticle, has been extensively studied in solution.[41-45] Non-classical crystallization has now become so established that several review papers [46-48] and a few books [3, 49] have been published and its tutorial and technical sessions were included respectively in the spring meetings of Materials Research Society (MRS) and European Materials Research Society (EMRS) in 2014. Hwang et al.[15, 16, 22] studied extensively the non-classical crystallization in the chemical vapor deposition (CVD) process. They suggested that charged nanoparticles are generated in the gas phase almost without exception under typical deposition conditions of CVD and become the building block of thin films and nanostructures. The liquid-like property of charged nanoparticles, by which the non-classical crystallization is made possible, is attributed to the weakening of bond strength by charge.

On the other hand, in the plasma enhanced CVD (PE-CVD) process, a concept

similar to non-classical crystallization was suggested by Cabarrocas, [12] Vladimirov and Ostrikov, [13] and Nunomura et al. [14]. Cabarrocas et al.[12, 50-52] suggested that the incorporation of nanocrystallites produced in the gas phase increased the film growth rate and the crystalline fraction and thereby improved transport properties and stability compared with hydrogenated amorphous Si (a-Si:H) films. They called such films polymorphous silicon films, which refer to a-Si:H matrix embedded with silicon nanocrystallites. Ostrikov [53, 54] made an extensive review on the incorporation of gas-phase nuclei into nanostructures for a reactive-plasma assisted nanoassembly process. Shiratani and his colleagues [55-58] measured the size distribution of nanoparticles generated in the gas phase under various conditions of PE-CVD using the time evolution of a laser light scattering (LLS) intensity.

In the plasma CVD process, the nanoparticles generated in the gas phase are known to be charged negatively because the mobility of electrons is much higher than that of ions in non-thermal plasmas.[59] And the negatively charged nanoparticles are expected not to escape from the sheath potential but to grow in the plasma. Therefore, negatively charged nanoparticles are not expected to contribute to deposition under normal deposition conditions. On the other hand, it is well established that microcrystalline films are deposited at low substrate temperature under typical processing conditions of plasma CVD. From such deposition behavior, it can be inferred that some crystalline nanoparticles formed in the plasma should be incorporated into films. Since the substrate potential is always negative with respect to the plasma, these nanoparticles are expected to be

positively charged.

In relation to the possibility for the formation of positively charged nanoparticles, based on the fact that some nanoparticles in the plasma grow so rapidly, Shiratani et al.[58] predicted that both positively and negatively charged nanoparticles should coexist. By placing a grounded grid in the plasma, Cabarrocas et al.[60, 61] showed that the deposition rate was decreased as the positive bias voltage on the substrate was increased in the capacitive coupled plasma CVD (CCP-CVD) process. This result means that positively charged nanoparticles are repelled by the positive bias on the substrate, indicating the presence of positively charged nanoparticles. Therefore, both positively and negatively charged nanoparticles are expected to coexist abundantly in the gas phase of the plasma CVD process.

However, only a little attention has been paid to the generation of positively charged nanoparticles and their role in deposition in the plasma CVD process. Positively and negatively charged nanoparticles would differ in their size, amount and crystallinity in the plasma CVD process. Therefore, the growth rate as well as crystallinity can be different depending on whether positively or negatively charged nanoparticles are deposited. It would be important to understand how to control the deposition of positively or negatively charged nanoparticles formed in the plasma.

The purpose of this work is to compare the deposition behavior between positively and negatively charged nanoparticles by applying the substrate bias. This

comparison is difficult under typical plasma CVD conditions because the plasma potential tends to vary with the substrate potential. By making the substrate size small enough, we could keep the plasma potential not to vary with the substrate potential and study the effect of the substrate on the deposition behavior of charged nanoparticles. By examining the deposition behavior on the substrate negatively biased, we could clarify the existence of positively charged nanoparticles and their role in the formation of crystalline films during plasma CVD.

2. EXPERIMENTS

When the bias is applied to the substrate under typical deposition conditions of Si in the inductively coupled plasma (ICP) CVD process, the plasma potential varies in proportion to the applied bias because there exists a sheath potential between the plasma and the substrate. This aspect is shown for the stainless steel substrate of 20 cm in diameter in figure 7. For this reason, the potential difference between the plasma and the substrate does not vary markedly with the substrate bias. As a result, the substrate bias does not show a pronounced effect on the deposition behavior. In other words, regardless of the applied bias, the substrate potential is always negative with respect to the plasma. For example, even though a substrate bias is positive, the negatively-charged species would not be attracted toward the substrate. For the substrate bias to have a pronounced effect, the size of the substrate should be so small that the plasma potential may be maintained not to vary with the substrate bias. This aspect is shown for the small stainless steel substrate of 3×5 mm² in figure 7.

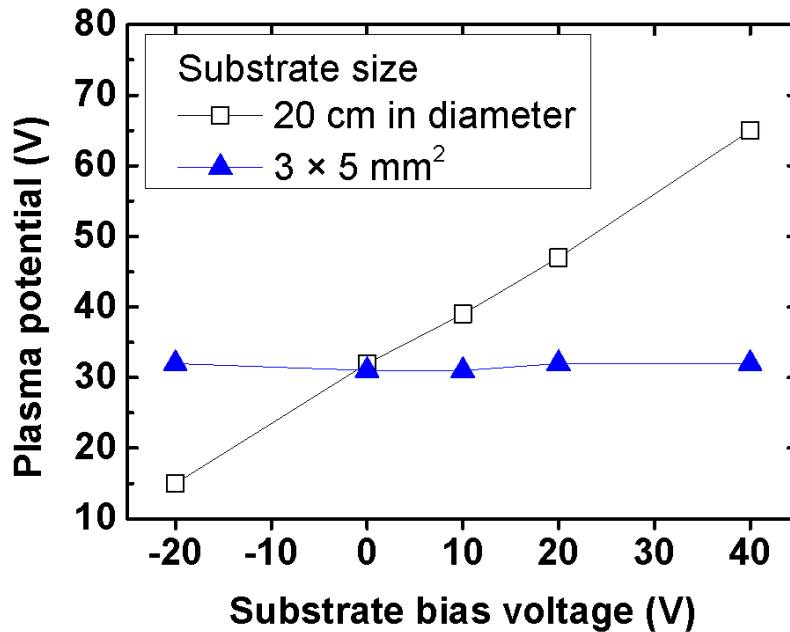


Figure 7. Plasma potentials measured with various bias voltages which were applied to a substrate of 20 cm in diameter (data of unfilled squares) and a small substrate of $3 \times 5 \text{ mm}^2$ (data of filled triangles).

Si thin films were deposited in a radio frequency (RF, 13.56 MHz) ICP-CVD reactor at a power of 1400 W. The cylindrical ICP-CVD reactor has a diameter of 37 cm with the diameter of the ring-type showerhead being 24 cm. The plasma was generated by a coil type antenna with diameter of 20 cm placed on a quartz window. The substrate was located 14 cm below the antenna, being at room temperature. The deposition time was 4 min and the reactor pressure was 350 mTorr. The flow rates of SiH_4 and H_2 were respectively 5 and 45 standard cubic centimeter per minute (sccm), which corresponds to a gas mixture of 10% SiH_4 -90% H_2 .

Si thin films were preliminarily deposited on a small p-type silicon wafer of 3×5 mm² at substrate biases of -10 V and 40 V as shown in FE-SEM images of figure 8(a) and 8(b), respectively. The morphology and thickness of Si films in figure 8(a) and 8(b) are different, indicating that the substrate bias has some effect on the deposition behavior. However, it should be noted that the doped Si wafer can be dielectric at room temperature because doping by ion implantation is done only at the surface, which is conducting, whereas the other part of the wafer is intrinsic and dielectric at room temperature. Since electric charges can be accumulated on the dielectric substrate in the plasma CVD process, the actual substrate potential can be different from the bias applied to the substrate. Therefore, the Si wafer substrate is not appropriate for the study of the bias effect on the deposition behavior. For this reason, graphite, which is conducting and minimizes the charge accumulation, is used as a substrate. It should be noted that the stainless steel substrate is inappropriate for this experiment because it cannot be fractured for the cross-section observation of the films by FE-SEM.

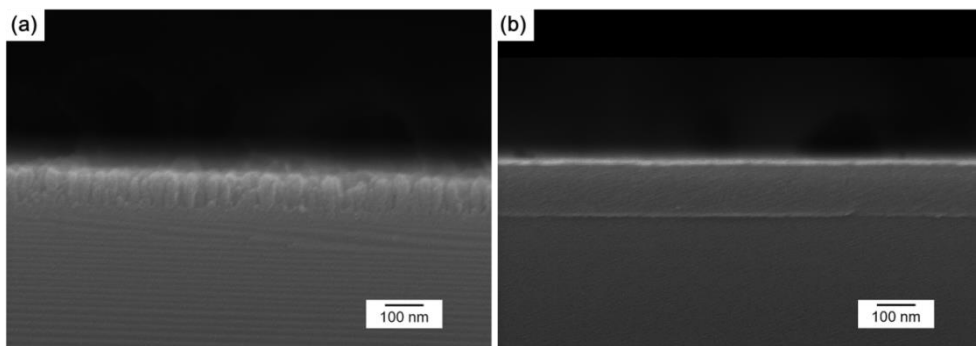


Figure 8. Cross-sectional FE-SEM images of Si films deposited for 4 min on p-type

silicon wafer at substrate biases of (a) -10 V and (b) 40 V.

To measure the plasma potential, V_p , and the electron temperature, a RF compensated Langmuir probe was used. The Langmuir probe consisted of a tungsten tip 3 mm long and 0.15 mm in diameter and a floating reference probe for reducing RF noise. The microstructure and deposition rate of Si films were investigated from the cross-section field emission scanning electron microscopy image (FE-SEM, S-4800, Hitachi, Japan). The crystallinity of deposited films was analyzed using a Raman spectrometer (LabRam HR-800, Horiba Jobin Yvon). To analyze Si nanoparticles in the gas phase, Si nanoparticles were captured on a carbon membrane of Cu grids for transmission electron microscope (TEM) under the same condition as the Si film deposition and then observed by high resolution transmission electron microscope (HR-TEM, Tecnai G2 F30, FEI, USA)

3. RESULTS AND DISCUSSION

Figure 9 shows the bias effect on the deposition rate of the Si films deposited on graphite for 4 min under the reactor pressure of 350 mTorr when the substrate bias was varied from -10 to 40 V. The deposition rates were 0.49, 0.53, 0.57, 0.36 and 1.5 nm/s respectively for the substrate biases V_s of -10, 10, 20, 30, and 40 V. The deposition rate at V_s of 40 V is about three times higher than those at V_s of -10, 10, 20 and 30 V. As shown in figure 7, the plasma potential V_p was maintained at ~ 32 V when the bias voltage of the small substrate ($3 \times 5 \text{ mm}^2$) was varied from -20 to 40 V. Thus, at the substrate bias of 40 V, the potential difference of 8 V exists

between the plasma and the substrate and negatively charged species would be accelerated from the plasma to the substrate and at the same time positively charged species are repelled from the substrate. On the contrary, at the substrate biases, V_s , of -10, 10, 20, and 30 V, the potential difference would be respectively, - 42, - 22, -12 and - 2 V between the plasma and the substrate and positively charged species would be accelerated toward the substrate and at the same time negatively charged species are repelled from the substrate.

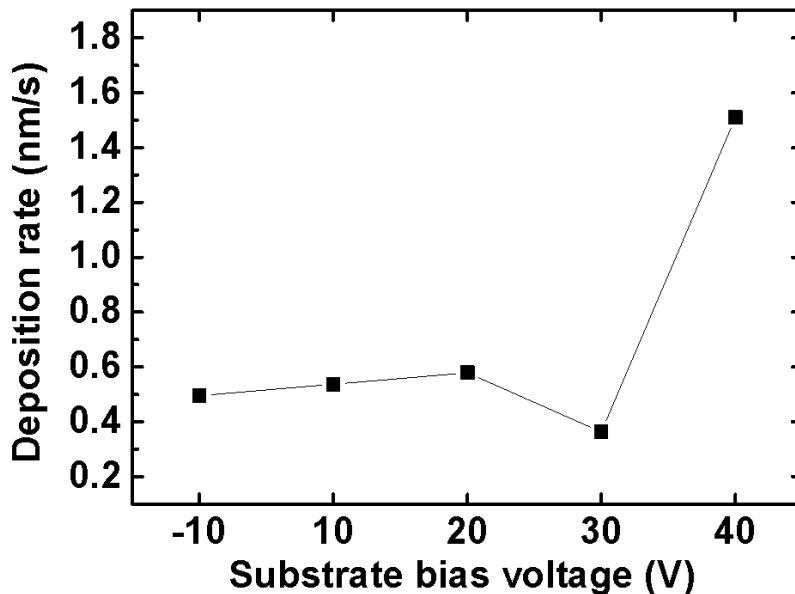


Figure 9. Deposition rates of Si films deposited for 4 min with various substrate biases from -10 V to 40 V.

On the other hand, the nucleation in the gas phase is known to occur extensively in the plasma CVD process and these nuclei are charged positively and negatively.[30, 51, 58, 62] Once the gas phase nucleation occurs extensively, the

total surface area of numerous nuclei is huge and the driving force for precipitation is consumed considerably. Usually, the remaining gas would have only negligible supersaturation for further precipitation and would negligibly contribute to deposition on a substrate at room temperature. This means that the deposition flux is mainly either positively or negatively charged nanoparticles and the deposition flux by neutral gas atoms or molecules would be negligibly small.

Considering that a major depositing flux is either positively or negatively charged nanoparticles, the depositing flux under the biases of -10, 10, 20 and 30 V would be mostly positively charged nanoparticles and the flux under the bias of 40 V would be mostly negatively charged nanoparticles in figure 9. The abrupt increase of the deposition rate under the bias of 40 V in figure 9 indicates that the negatively charged nanoparticles are much larger than that of the positively charged ones in the silane ICP-CVD process. More specifically, since the deposition rate of the film deposited under 40 V is about three times higher than those deposited under -10, 10, 20 and 30 V, the amount of negatively charged nanoparticles would be about three times larger than that of positively charged nanoparticles.

Hereafter, let us examine deposition rates in the range of V_s from -10 to 30 V. In this range, the deposition rates are varied much smaller than those in the range of V_s from 30 to 40 V. The floating potential V_f of the substrate, which has a potential lower than the plasma potential by the sheath potential difference, was measured to be ~ 23 V by the single Langmuir probe when the substrate was not biased. At V_f of ~ 23 V, the fluxes of positive and negative species incoming to the

substrate become the same with the charge being in equilibrium. When the substrate is biased, however, the floating potential changes to the substrate bias and the new equilibrium would be set up. Therefore, when the substrate bias is lower than ~ 23 V, incoming positive and negative species would increase and decrease, respectively. Likewise, when the substrate bias is higher than ~ 23 V, incoming positive and negative species would respectively decrease and increase. And incoming species with lower mass is more likely to be increased or decreased sensitively than heavier species by their mobility difference as the substrate potential changes from ~ 23 V. Therefore, depending on whether the substrate is lower or higher than ~ 23 V, the deposition behavior could be influenced by the species such as electrons or ions, which have higher mobility than nanoparticles. As V_s increase from 23 to 30 V, electrons, which are lowest in mass among negatively charged species, would be strongly influenced by the above aspect. In this situation, it is expected that the sheath length becomes smaller as the sheath potential decreases.[63, 64]

Considering that the potential differences between the plasma and the substrate for V_s of 30 and 20 V are -2 and -12 V respectively, the sheath length for V_s of 30 V would be shorter than that of V_s of 20 V, which would decrease the effective collection area. Because of this decreased collection area, the flux of positively charged nanoparticles would be decreased, decreasing the deposition rate at V_s of 30 V. This would be why as V_s increased from 20 to 30 V, the deposition rate decreased from 0.57 to 0.36 nm/s in figure 9.

Meanwhile, in the range of V_s from 20 to -10 V, the deposition rates decreased as V_s decreased in contrast with the deposition rate in the range of V_s from 20 to 30 V. To understand this deposition behavior, it should be noted that the flux of positively charged species does not increase continuously as V_s decreases with respect to V_p . Instead, the flux of positively charged species will be saturated because the mobility of positively charged species is much lower than that of electrons. However, figure 9 shows that the deposition rate was rather decreased as V_s decreased from 20 to -10 V. This decrease of the deposition rate might be attributed to the bombardment of energetic ions inhibiting the deposition of positively charged nanoparticles into the films, which seems to be pronounced at the high potential difference between the plasma and the substrate.[65, 66]

Figure 10 shows the cross-sectional FE-SEM images of Si thin films in figure 9. The films deposited with V_s from -10 to 30 V have a typical columnar structure (figure 10(a)-10(d)) whereas the film deposited with V_s of 40 V is not columnar but more like a powder compact (figure 10(e)). Considering that the potential difference between the plasma and substrate would be -42 , -22 , -12 , -2 and 8 V respectively in figure 10(a)-10(e) as explained above, positively charged nanoparticles would be deposited in figure 10(a)-10(d) and negatively charged flux would be deposited in figure 10(e). The columnar and non-columnar structures in figure 10 may not be explained merely by the polarity difference of the depositing flux. They may be related to the potential difference between the plasma and the substrate and the size of charged nanoparticles. For example, if negatively charged

nanoparticles are larger than positively charged nanoparticles, their mobility toward the substrate would be relatively low, which may result in the non-columnar structure of figure 10(e). The mobility of positively charged nanoparticles, whose size is relatively small, would be relatively high toward the substrate, which may result in the columnar structure of figure 10(a)-(d). For the information of the crystallinity and crystallite size of the films in figure 10, the films were analyzed by Raman spectroscopy.

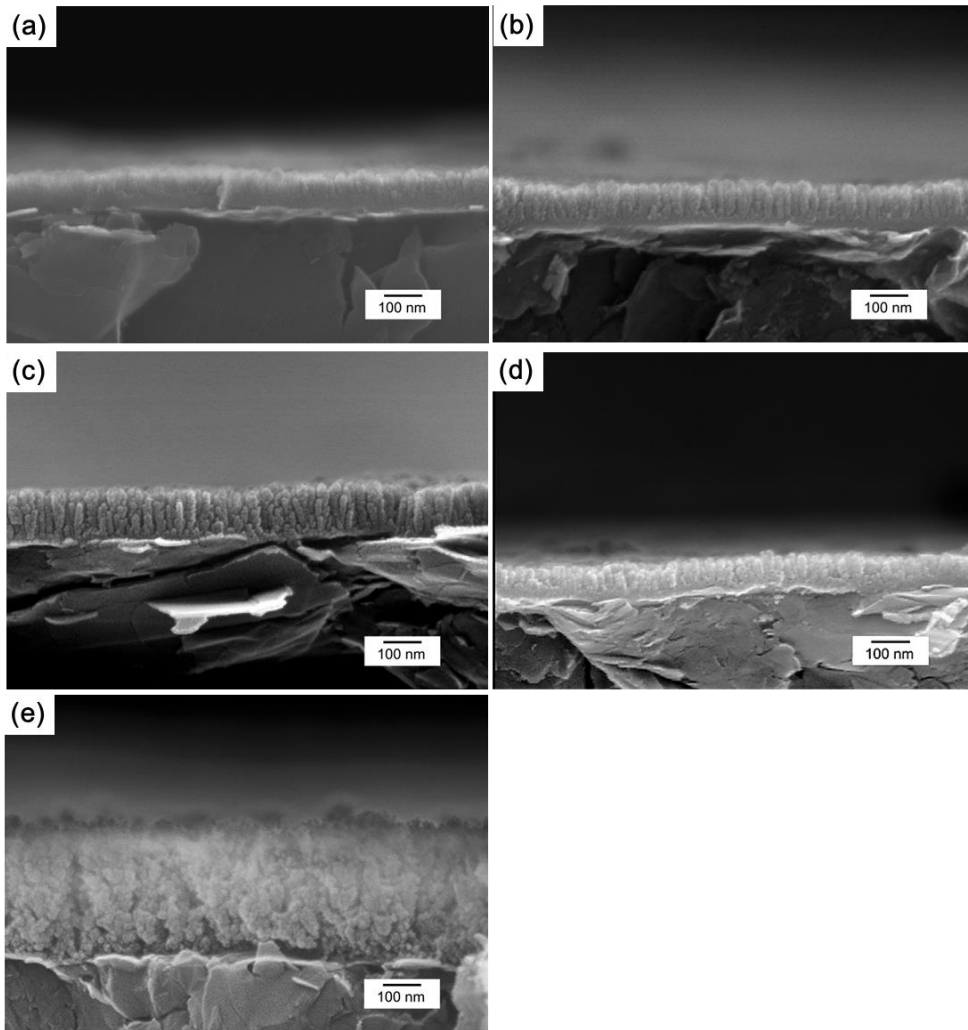


Figure 10. Cross-sectional FE-SEM images of Si films deposited for 4 min on a graphite substrate at substrate biases of (a) -10 V, (b) 10 V, (c) 20 V, (d) 30 V, and (e) 40 V.

Figure 11 shows the Raman spectra of Si films prepared under the same conditions as the samples in figures 9 and 10. Although the substrate was near room temperature, figure 11 indicates that the films have some crystallinity which can be verified by transverse optic (TO) peaks of nanocrystalline phase centered at 519 cm^{-1} for V_s of 40 V and 516 cm^{-1} for V_s of $-10 \sim 30$ V, respectively. The standard TO peak for crystalline Si is at 520 cm^{-1} . The shift of TO peak from 520 cm^{-1} to the lower wave number is attributed to the decrease of crystallite size. Based on the schemes reported by Chaâbane and Suendo et al.[61], the size of nanocrystallites is estimated from the Raman result. The estimated size of Si nanocrystallites is $\sim 8\text{ nm}$ for V_s of 40 V and $\sim 3\text{ nm}$ for V_s of $-10 \sim 30$ V. These sizes of nanocrystallites will be confirmed by TEM in figure 12 and 13.

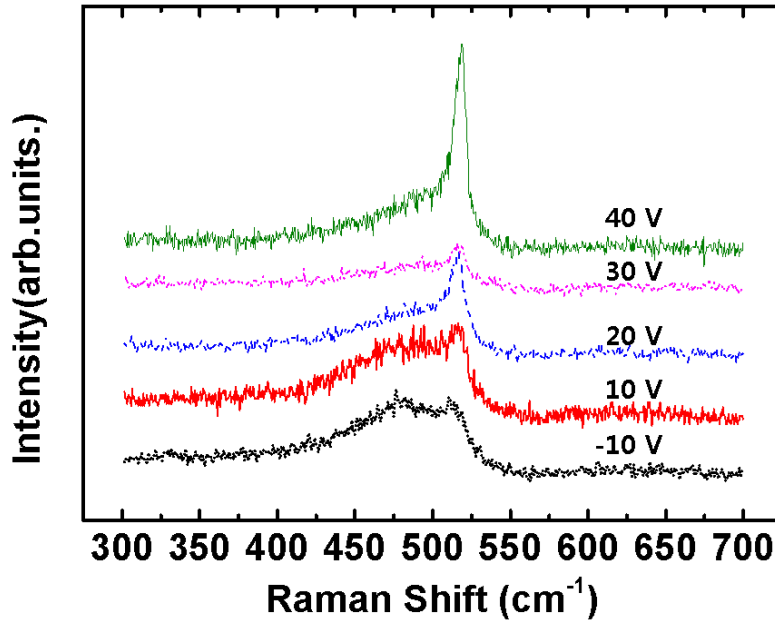


Figure 11. Raman spectra of Si films deposited at the same conditions as in Figure 9. Crystalline volume fractions were estimated as 0.84, 0.59, 0.56, 0.24, and 0.12 at substrate biases of 40, 30, 20, 10, and -10 V, respectively.

From the Raman spectra in figure 11, crystalline volume fractions of the films are determined by the equation, $X_c = (I_{nc} + I_m) / (I_{nc} + I_m + I_a)$ using the scheme of the previous report.[67] Here, I_{nc} , I_m , and I_a are the integrated intensities of bands of nanocrystalline, intermediate, and amorphous phase, respectively, where the bands are deconvoluted from the Raman spectra in figure 11 into crystalline (~ 516 cm^{-1} and ~ 516 cm^{-1}), amorphous (480 cm^{-1}) and intermediate (~ 507 cm^{-1}) bands. The crystalline fractions were estimated to be 0.12, 0.24, 0.56, 0.59 and 0.84 respectively at V_s of -10 , 10, 20, 30 and 40 V.

Considering that the diffusivity of Si is negligible near room temperature, the crystalline phase in films of figure 11 cannot be formed by the atomic or molecular diffusion on the substrate or the growing surface. It is most likely that the crystalline nanoparticles should have formed in the gas phase and be incorporated into the films. Besides, these nanoparticles would be charged either positively or negatively in the plasma environment. The following three facts should be noted. First, as mentioned earlier, the main depositing flux is nanoparticles. Second, the substrate is near room temperature. Third, the Raman spectra in figure 11 indicate that the films consist of both amorphous and crystalline phases. Considering these facts, it can be deduced that some charged nanoparticles are crystalline and others are amorphous in the gas phase.

To examine the detailed microstructure of the films deposited at V_s of 10 V (figure 10(b)) and 40 V (figure 10(e)), cross-sections of the Si films were observed by HR-TEM as shown in figure 12. Figure 12(a) and 12(b) show respectively low and high magnification images of the film deposited at V_s of 40 V. Figure 12(c) and 12(d) show respectively low and high magnification images of the film deposited at V_s of 10 V. Judging from the lattice fringe, figure 12(b) shows relatively larger nanocrystallites embedded in the amorphous matrix than those of figure 12(d).

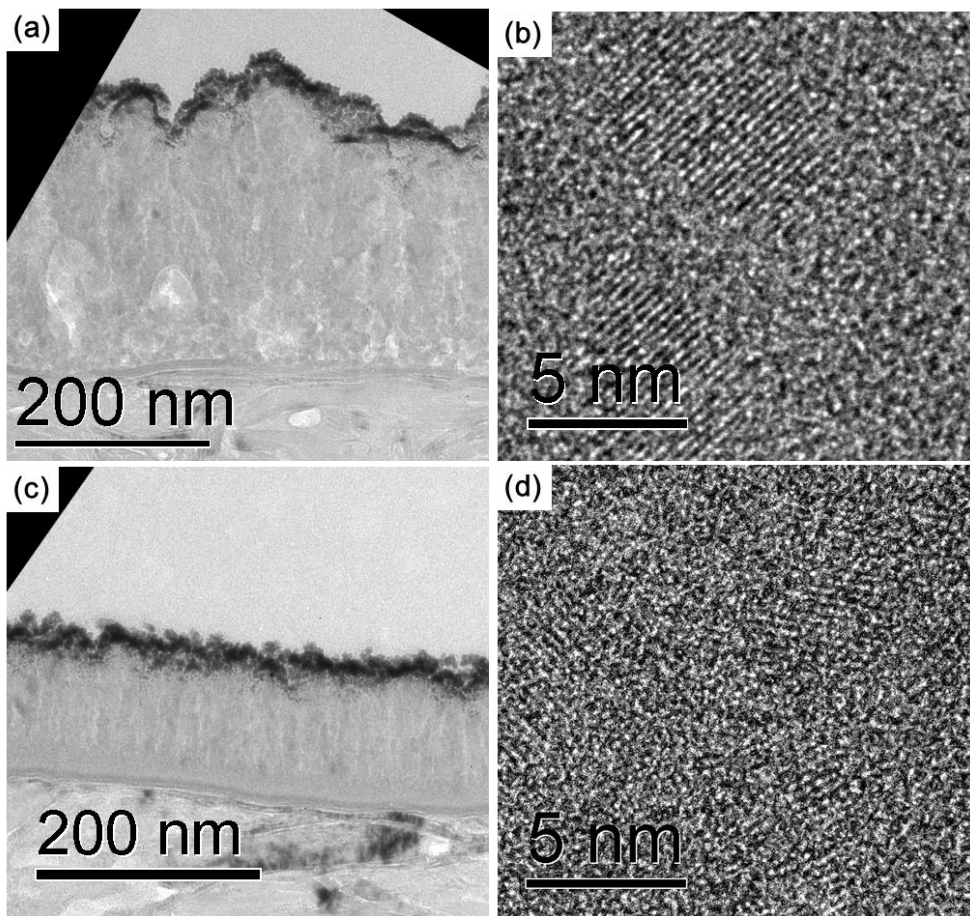


Figure 12. Cross-sectional TEM images for Si films prepared at substrate biases of (a) 40 V and (c) 10V at the same conditions as in Figure 9. Images of (b) and (d) are high-resolution images of (a) and (c), respectively.

For further investigation, Si nanoparticles in the gas phase were captured on the TEM grid membrane, which was placed on the graphite substrate biased at V_s of 40 V and 10 V and observed by HR-TEM as shown respectively in figures 13(a) and 13(b). In figure 13(a), the crystalline nanoparticles, which were captured for 15 sec, have the size range of 6 ~ 13 nm, which roughly agrees with ~ 8 nm determined by Raman spectra in figure 11. In figure 13(b), the crystalline nanoparticles, which

were captured for 25 sec, have the size range of 3 ~ 6 nm, which roughly agrees with ~ 3 nm determined by Raman spectra in figure 11. The size of nanoparticles in figure 13(a) and 13(b) also agrees respectively with the size of nanocrystallites in figure 12(b) and 12(d). The capture times of 15 sec in figure 13(a) and 25 sec in figure 13(b) were chosen to deposit a 10 nm-thick layer of Si, which is necessary for the anti-oxidation of small nanoparticles below the size of 3 nm.[68] The nanoparticles of ~ 3 nm were also observed in plasma CVD by other groups.[61, 68] Using the grid in the conductively-coupled plasma CVD process, Chaâbane et al. and Cabarrocas et al.[61, 69] applied the positive bias to the substrate with respect to the grid. They observed that the deposition rate decreased with increasing positive bias. Based on this observation, they suggested that positively-charged nanoparticles are generated in the plasma CVD process.

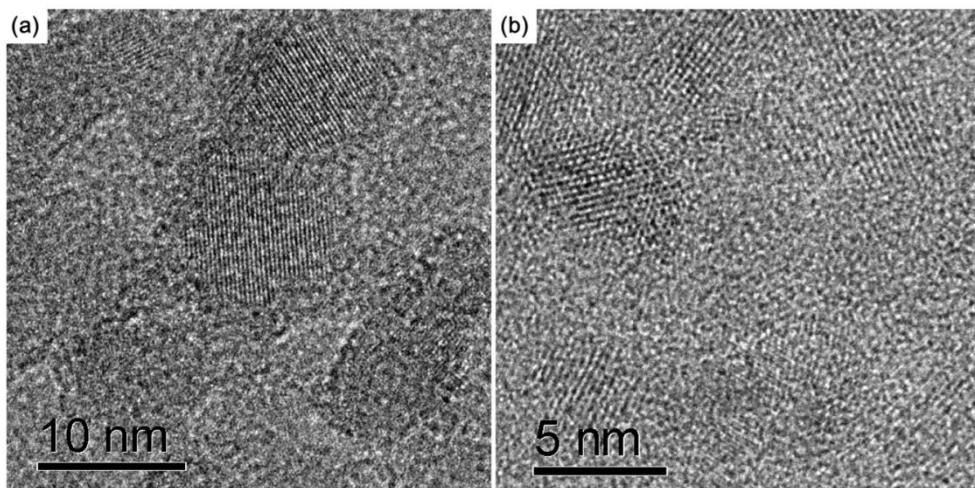


Figure 13. Plane view high-resolution TEM images of Si nanoparticles captured on the membrane of TEM grids at substrate biases of (a) 40 V and (b) 10 V.

Figure 13(a) shows that negatively-charged nanoparticles are in the size range of 6 ~ 13 nm. These nanoparticles would be the depositing flux of the film in figure 10(e). Since the film in figure 10(e) has the crystalline fraction of 0.84, which was estimated from the Raman spectra in figure 11, most of these negatively charged nanoparticles appear to be crystalline and only a minor percentage of them appears to be amorphous. Figure 13(b) shows that positively-charged nanoparticles are in the size range of 3 ~ 6 nm. These nanoparticles would be the depositing flux of the films in figures 11(a)-11(d). However, the crystalline fractions of the films in figures 11(a)-11(d) increased with increasing V_s being respectively 0.12, 0.24, 0.56, and 0.59. In order to explain the increased crystalline fraction with increasing V_s , it must be assumed that positively-charged nanoparticles of 3 ~ 6 nm should undergo transition from a crystalline to an amorphous phase upon landing on a growing surface and this tendency becomes stronger with decreasing V_s or increasing potential difference between the plasma and the substrate. In relation to this possibility, Hwang et al. suggested that charged nanoparticles have a liquid-like property with the tendency increasing with decreasing size because the charge weakens the bond strength. If charged nanoparticles with a liquid-like property are accelerated toward the substrate by the potential difference between the plasma and the substrate, the transition from a crystalline to amorphous phase would be enhanced with increasing potential difference, resulting in the decrease of the crystalline fraction.

4. CONCLUSION

Using a graphite substrate so small that the plasma potential was not varied with the substrate bias, the substrate bias was shown to have a definitive effect on the deposition behavior of charged nanoparticles in the ICP-CVD process. Both positively and negatively charged crystalline nanoparticles were shown to exist in abundance in the gas phase with the negatively-charged ones being larger than the positively-charged ones. If the positive bias higher than the plasma potential was applied to the substrate, the negatively charged nanoparticles could be made to deposit, which resulted in the highest film growth rate and the highest crystalline fraction. According to this study, the reason why crystalline silicon films can be deposited on a substrate at such low temperature as the silicon diffusivity is negligibly low is that positively charged crystalline nanoparticles, which are formed in the plasma, are accelerated by the sheath potential difference toward the growing surface of films in typical PE-CVD processes.

Chapter III. Application of Charged Nanoparticles Theory in ICP-CVD process: Enhancement of Generation of Positively Charged Nanoparticles

1. INTRODUCTION

The formation of crystallites in the microcrystalline or polycrystalline silicon films have been not understood in the plasma enhanced chemical vapor deposition process because the gas temperature of nonthermal plasmas is not sufficient to generate crystalline silicon.[70] Although the reason of generation of Si crystal is unclear, the study on the incorporation of crystalline nanoparticles into the film has been established to obtain the Si film having high deposition rate and high structural quality.[11, 71]

In nonthermal plasmas, it is mostly regarded that nanoparticles generated in the gas phase are charged negatively because the mobility of electrons is much higher than that of ions in non-thermal plasmas.[59, 72] However, the negatively charged nanoparticles are expected not to escape from the sheath potential and to trapped in the plasmas, the negatively charged nanoparticles cannot be the main building block of crystalline films. Therefore nanoparticles should be charged positively to incorporate to the film on substrate after generation in plasmas. From this expectation, experimental evidences of presence of positively charged NPs were studied [58, 61] and theoretical explanations were calculated by simulation[73]. To achieve high deposition rate and high crystalline volume fraction during the Si film

deposition in the plasma CVD process, it is necessary to know why the positively charged nanoparticles are generated and how the generation of positively charged nanoparticles is enhanced in plasmas.

Among the mechanisms about positive charging of nanoparticles, secondary electron emission is one of the reliable explanations.[73, 74] If secondary electrons are emitted from the nanoparticles, the nanoparticles are expected to be charged positively. And, for the secondary electron emission from silicon nanoparticles, it is reported that high magnitude of electric field is needed.

According to the previous result, near the RF antenna, there is high magnitude of electric field.[75] Therefore the positively charged nanoparticles can be generated in the area near the RF antenna. The purpose of this study is to investigate generation of positively charged nanoparticles by change of silane feeding position near the RF antenna.

2. EXPERIMENTS

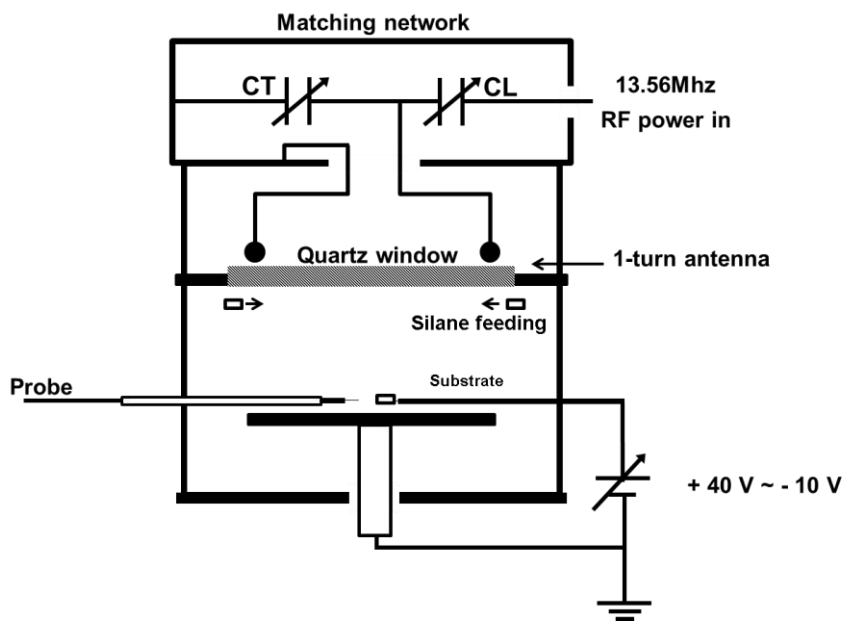


Figure 14. Schematic of the experimental setup

Si thin films were deposited in a radio frequency (RF, 13.56 MHz) ICP-CVD reactor at a power of 1400 W. The plasma was generated by a coil type antenna with diameter of 20 cm placed on a quartz window. The cylindrical ICP-CVD reactor has a diameter of 37 cm and the various diameter of the ring-type showerhead being 30, 24, 10, 0 cm were used to change silane feeding position. The feeding silane by showerhead of 0 cm in diameter indicates injection of silane at the center of chamber by a tube. The substrate was located 14 cm below the antenna, being at room temperature. The deposition time was 4 min and the reactor pressure was 350 mTorr. The flow rates of SiH_4 and H_2 were respectively 5 and 45 standard cubic centimeter per minute (sccm), which corresponds to a gas mixture of 10% SiH_4 -90% H_2 .

To measure the plasma potential, V_p , and the electron temperature, a RF compensated Langmuir probe was used.[76] The Langmuir probe consisted of a tungsten tip 3 mm long and 0.15 mm in diameter and a floating reference probe for reducing RF noise. The microstructure and deposition rate of Si films were investigated from the cross-section field emission scanning electron microscopy image (FE-SEM, S-4800, Hitachi, Japan). The crystallinity of deposited films was analyzed using a Raman spectrometer (LabRam HR-800, Horiba Jobin Yvon). Cross-sectional TEM specimens of silicon films were prepared either using focused ion beam (FIB, SMI3050SE, SII Nanotechnology, Japan), and then observed by high resolution transmission electron microscope (HR-TEM, Tecnai G2 F30, FEI, USA)

Substrate bias was used to attract positively or negatively charged nanoparticles toward the substrate depending on the potential difference between the plasma potential and the substrate. As we shown the figure 7, applying DC biases on a large area of substrate can change the plasma potential so that the substrate bias effect cannot be verified. Therefore we used small graphite substrate of small stainless steel substrate of $3 \times 5 \text{ mm}^2$ in figure 7. As we shown the figure 7, applying DC biases on the small substrate did not change the plasma potential.

3. RESULTS AND DISCUSSION

Figure 15 shows the cross-sectional FE-SEM images of Si thin films deposited on the graphite substrate for the substrate bias of -10 V under the reactor pressure

of 350 mTorr, when the diameter of showerhead was (a) 30, (b) 24, (c) 10, (d) 0 cm, respectively. The plasma potential was measured to be ~ 32 V, and the potential difference between the plasma and the substrate was -42 V. Therefore, in the potential difference between the plasma and the substrate, the positively charged nanoparticles were deposited. The deposition rate of the films deposited at substrate bias of -10 V is increased as the diameter of showerheads is decreased from 30 to 0 cm. This result indicates that the generation of positively charged nanoparticles was increased as the diameter of showerheads is decreased from 30 to 0 cm.

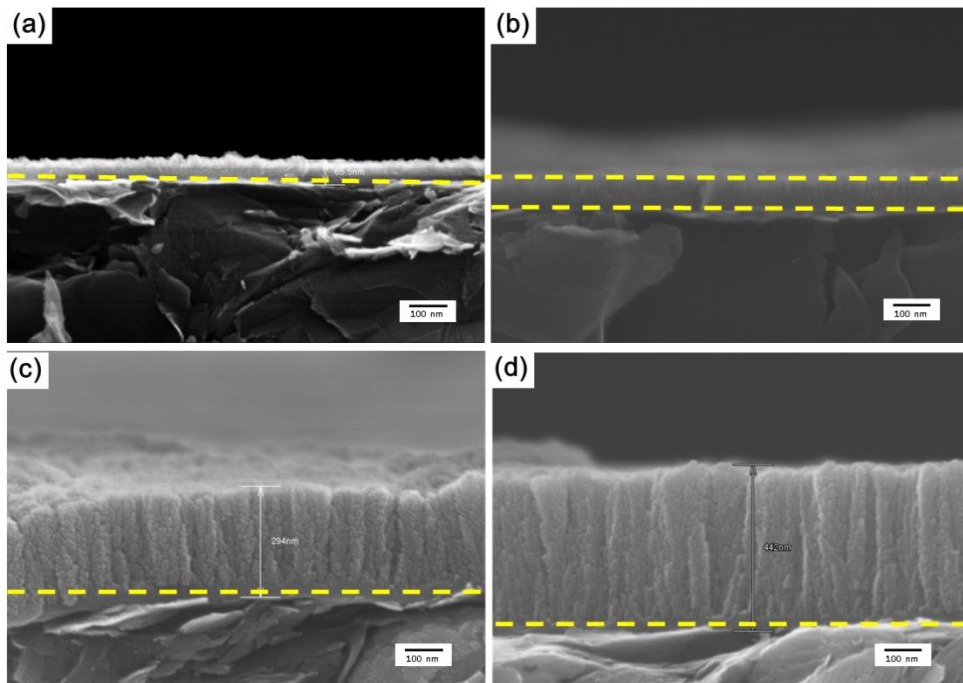


Figure 15. Cross-sectional FE-SEM images of Si thin films deposited on graphite for 4 min under the reactor pressure of 350 mTorr with the showerhead of (a) 30, (b) 24, (c) 10, (d) 0 cm in diameter when the substrate bias was -10 V.

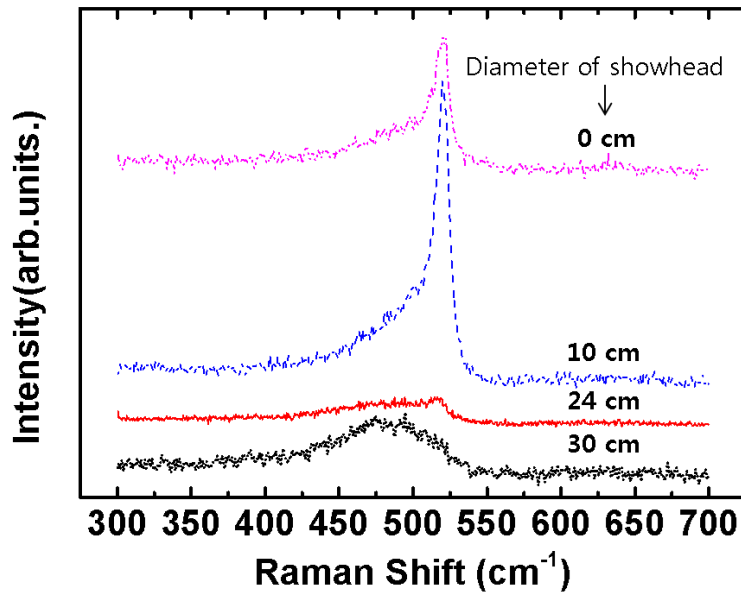


Figure 16. Raman spectra of Si films deposited at the same conditions as in figure 15.

Figure 16 shows the Raman spectra of Si films prepared under the same conditions as in figures 15. In figure 16, the films showing transverse optic (TO) peaks of nanocrystalline Si phase centered at 516 cm^{-1} have some crystallinity. The standard TO peak for crystalline Si is at 520 cm^{-1} . And the shift of TO peak from 520 cm^{-1} to the lower wave number is attributed to the decrease of crystallite size.

From the Raman spectra in figure 16, bands are deconvoluted from the Raman spectra in figure 16 into crystalline ($\sim 518\text{ cm}^{-1}$ and $\sim 516\text{ cm}^{-1}$), amorphous (480 cm^{-1}) and intermediate ($\sim 507\text{ cm}^{-1}$) bands, crystalline volume fractions of the films are determined by the equation, $X_c = (I_{nc} + I_m) / (I_{nc} + I_m + I_a)$. Here, I_{nc} , I_m , and I_a are the integrated intensities of bands of nanocrystalline, intermediate, and amorphous

phase, respectively. The crystalline fractions were estimated to be 0, 0.12, 0.80, and 0.87 when the diameter of showerhead was (a) 30, (b) 24, (c) 10, (d) 0 cm respectively.

The films in figure 15 (b - d) have crystalline phase though the substrate was near room temperature. Considering that the diffusivity of Si is so low at room temperature, the crystalline phase in films of figure 15 cannot be formed by the atomic or molecular diffusion on the substrate. It is more likely that the crystalline nanoparticles was formed in the gas phase and incorporated into the films.

Furthermore, since the negatively charged nanoparticles are expected not to escape from the sheath potential, the increase of deposition rate of films in the figure 15 means that generation of positively charged nanoparticles were enhanced depending change of silane feeding position.

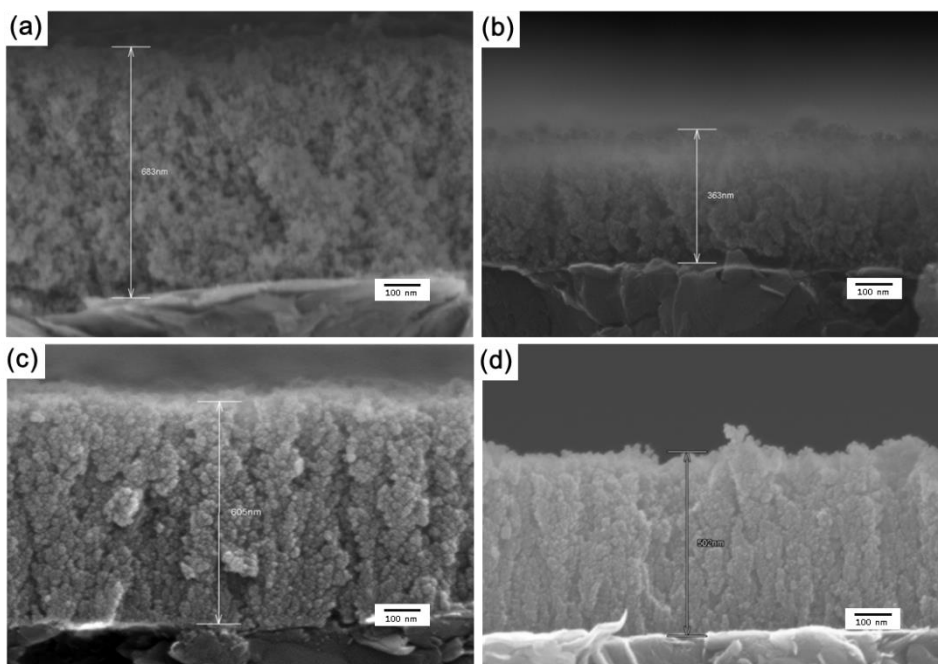


Figure 17. Cross-sectional FE-SEM images of Si thin films deposited on graphite for 4 min under the reactor pressure of 350 mTorr with the showerhead of (a) 30, (b) 24, (c) 10, (d) 0 cm in diameter when the substrate bias was 40 V.

Figure 17 shows the cross-sectional FE-SEM images of Si thin films deposited on graphite for 4 min under the reactor pressure of 350 mTorr with the showerhead of (a) 30, (b) 24, (c) 10, (d) 0 cm in diameter when the substrate bias was 40 V. The films deposited for substrate bias of 40 V with showerheads of 30, 24, 10, 0 cm in diameter in figure 17 are thicker than the films deposited for the substrate bias of -10 V with showerheads of 30, 24, 10, 0 cm in diameter in figure 15 respectively. However difference of thickness between the films deposited with V_{sub} of -10 V and deposited with V_{sub} of 40 V is decreased as the diameter of the showerhead is decreased. This result indicates that electric polarity of charged nanoparticles is changed from negative to positive as the diameter of the showerhead is decreased.

Considering this result, it can be deduced that the generation of positively charged nanoparticles is related with the area under the RF antenna, where high magnitude of electric field exists.

4. CONCLUSIONS

As the diameter of the showerhead is decreased, the deposition rate and the crystallinity of the films deposited for substrate bias of -10 V is increased. Considering the fact that positively charged species are accelerated from the plasma to the substrate in the potential difference between plasma potential of 32 V and substrate bias of - 10 V, generation of positively charged nanoparticles is enhanced as the diameter of showerhead is decreased. Therefore, charging mechanism of positively charged nanoparticles is related with area under the RF where magnitude of electric field is larger than the other area of the plasma.

Chapter IV. Control of Nanoparticle Size and Their Amount by Using the Mesh Grid and the DC-Biased Substrate in Silane ICP-CVD Process

1. INTRODUCTION

Semiconductor nanoparticles have attracted much attention because of their applications in electronics devices such as light-emitting devices, photovoltaic devices, etc. Unlike bulk semiconductor materials, the bandgap of semiconductor nanoparticles are reported to depend on their size known as quantum confinement.[77] Therefore significant efforts have been made to apply the quantum confinement effect of nanoparticles on light-emitting diodes[78, 79], and photovoltaic cells[80, 81].

Among the semiconductors materials studied, group II–VI conductors and group IV–VI semiconductor have attracted a great attention due to their superior optical properties. However, in those compound semiconductors, toxic heavy metals such as cadmium selenide (CdSe) and lead selenide (PbSe) are used primarily. On the other hand, IV group elements have also attracted a great attention because the IV group elements are relatively free from the environmental issue so that it would be a good substitute for the toxic compound semiconductor. Among the groups IV elements, silicon has many advantages because silicon is

abundant in the earth's crust and already widely used in large area electronics.

Many synthesizing methods for silicon nanoparticles are established based on the nonthermal plasmas.[82-84] Because the nanoparticles synthesized in plasmas are expected to be charged [72] and be suppressed to agglomerate, they would remain in narrow size distribution[85, 86]. However, the synthesizing methods for silicon nanoparticles mostly use the tube reactor which is not applicable to the large area electronics.

In this paper, we synthesized crystalline Si nanoparticles in a planar plasma CVD chamber which can be applied to the large area electronics. And we adopted the grounded grid for obtaining nanoparticles as reported in the previous report[87]. Moreover, based on the fact the nanoparticles generated in the plasmas are charged, direct current (DC) biases are applied to the substrate to control nanoparticle sizes and their amount during plasma CVD.

2. EXPERIMENT

Figure 18 shows the schematic of the experimental setup. The planar ICP-CVD reactor has a diameter of 37 cm. To generate the radio frequency (RF, 13.56 MHz) plasma, RF power was coupled to a coil type antenna with a diameter of 20 cm placed on a quartz window.

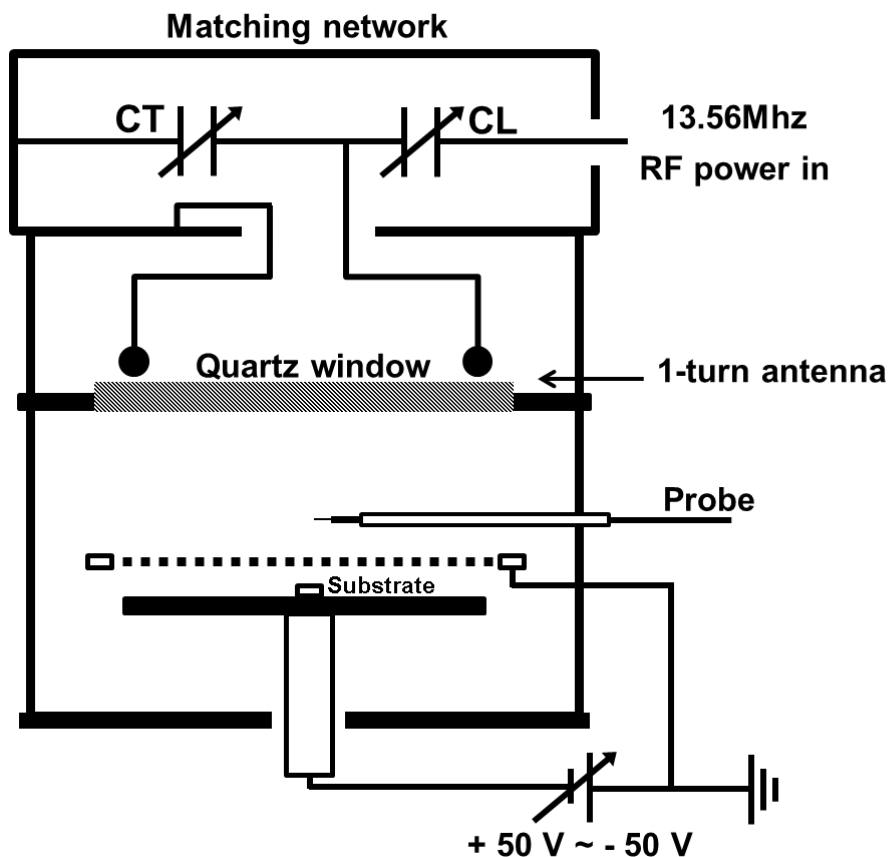


Figure 18. Schematic of the planar ICP chamber.

Si nanoparticles were deposited on the substrate with a gas mixture of 10%SiH₄-90%H₂ at a discharge power of 1400 W in the ICP-CVD reactor. The gas mixture was injected through the ring-type showerhead with a diameter of 30 cm, which was placed below the quartz window. The flow rates of SiH₄ and H₂ were respectively 5 and 45 standard cubic centimeter per minute (sccm) and the reactor pressure was 350 mTorr. A P-type silicon wafer was used as a substrate and placed on a stainless steel susceptor 14.5 cm below the power feed of the antenna. The substrate was at room temperature.

By inserting the grounded grid 5 mm above the substrate, Si nanoparticles were deposited on the substrate. The length of the square meshes of the grounded grid was 1 mm or 2 mm.

The size distribution of nanoparticles and their flux to the substrate were examined by the field emission scanning electron microscopy images (FE-SEM, S-4800, Hitachi, Japan) at four different points of the substrate. Si nanoparticles were deposited on a carbon membrane of Cu grids for transmission electron microscope (TEM) and then observed by high resolution transmission electron microscope (HR-TEM, Tecnai G2 F30, FEI, USA). To measure the plasma potential, V_p , a RF compensated Langmuir probe was used, which was placed 2 cm above grounded mesh grid.

3. RESULTS AND DISCUSSION

Figure 19 (a) and (b) show the FE-SEM images for the Si nanoparticles deposited on the grounded substrate for 30 seconds under the pressure of 350 mTorr at RF power of 1400 W. Si nanoparticles shown in figure 19 (a) and figure 19 (b) are synthesized with the grounded grid of 1 mm and 2 mm meshes, respectively. Figure 19 (c) and (d) show the TEM images for the Si nanoparticles prepared under the same conditions as those of figure 19 (a) and figure 19 (b), respectively. As shown in figure 19 (c) and figure 19 (d), the Si nanoparticles have crystallinity.

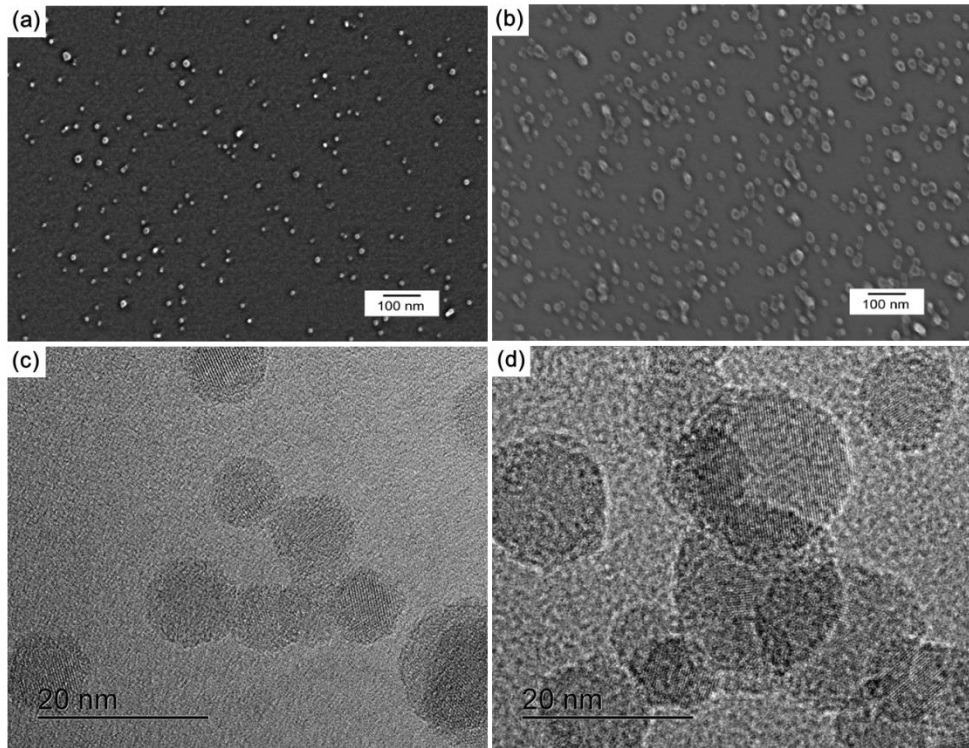


Figure 19. SEM images of Si Nanoparticles deposited on silicon wafer substrate at V_{sub} of 0 V with grounded grid of (a) 1 mm and (b) 2 mm meshes. High-resolution TEM images of Si nanoparticles deposited on the membrane of TEM grids at V_{sub} of 0 V with grounded grid of (c) 1 mm and (d) 2 mm meshes.

Considering the fact that the grounded grid separated its lower region from the plasma, the crystalline nanoparticles would not be formed below the grounded grid, but formed in the plasma above the grounded grid and then passed through the mesh of grounded grid. Crystalline nanoparticles tend to be self-assembled and form a film in the plasma CVD process. Therefore, to synthesize crystalline nanoparticles, their film formation in a plasma CVD process should be avoided. For this, crystalline nanoparticles are cooled and collected away from plasma

region.[88] On the other hand, the grounded grid can be used to produce crystalline nanoparticles because it separates the substrate from the plasma. If crystalline nanoparticles pass through the mesh of the grounded grid after their formation in the plasma region of the CVD reactor, they can be collected on the substrate. Therefore, crystalline nanoparticles can be collected or deposited on a substrate by using the grounded grid.

If the bias is applied to the substrate, the deposition behavior of Si nanoparticles would depend on their polarity. To study such deposition behavior, the bias applied to the substrate was varied from -50 V to $+50$ V with the 1 mm mesh grid under 350 mTorr at RF power of 1400 W and the deposition behavior is shown in Figure 20. As the substrate bias increased from -50 V to 0 V, the number density of nanoparticles is decreased as shown in Figure 20(a), (b) and (c). The diameter of Si nanoparticles of the highest frequency is in the range of 10 ~ 12 nm. At the substrate biases of $+25$ V and $+50$ V, however, nanoparticles did not deposit at all as shown in Figure 20(d) and (e). From the fact that the flux of deposited nanoparticles continues to decrease as the bias voltage increases from -50 V to 0 V and becomes zero at the biases of $+25$ V and $+50$ V, it can be inferred that Si nanoparticles should be positively charged. Especially, the result of non-deposition on the substrate applied with biases of $+25$ V and $+50$ V indicates that none of nanoparticles were negatively-charged.

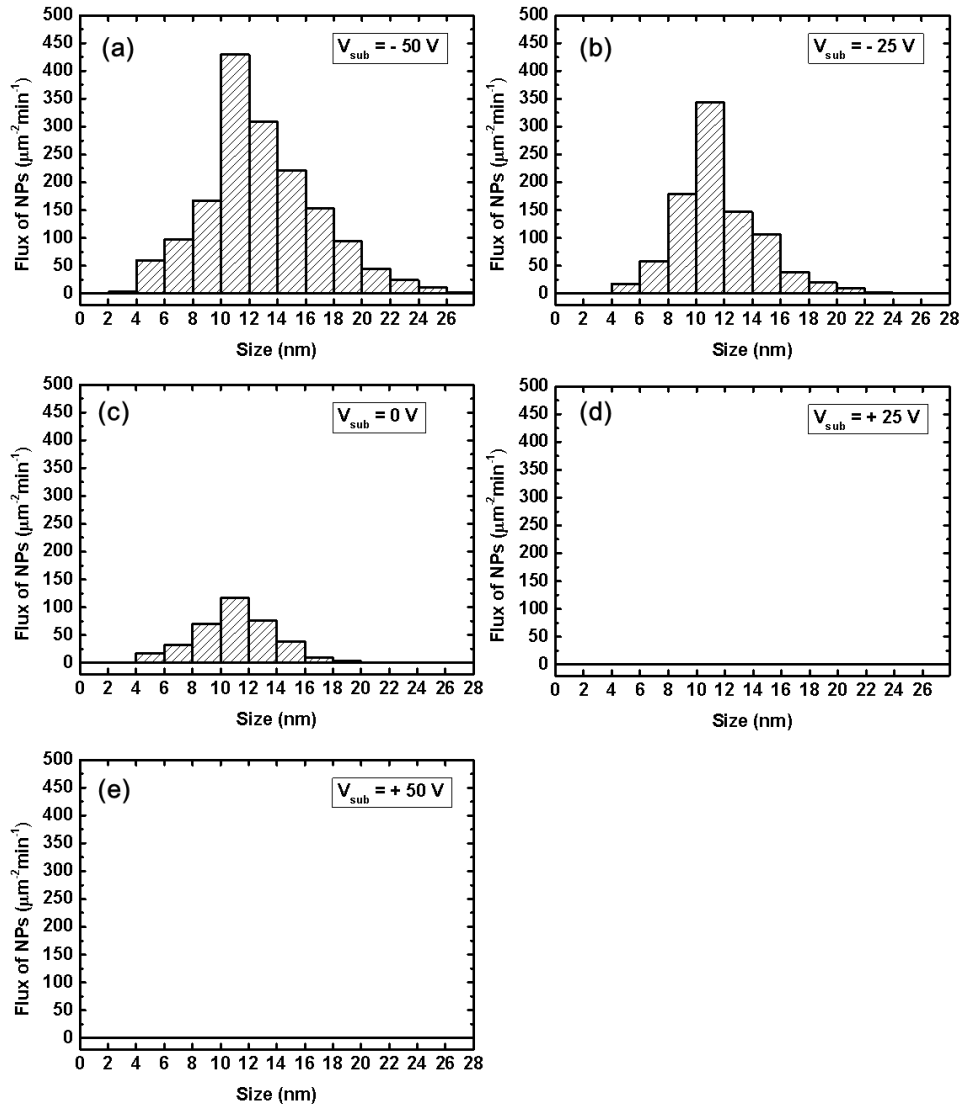


Figure 20. Size distributions and number density of Si nanoparticles for substrate bias of (a) -50, (b) -25, (c) 0, (d) + 25, and (e) + 50 V with grounded grid of 1 mm meshes at RF power of 1400 W.

In relation to the possibility for the generation of positively-charged nanoparticles in the plasma CVD process, Shiratani and his colleagues [58] predicted their presence from the unusually high growth rate of nanoparticles,

which cannot be explained without positively charged nanoparticles. And Cabarrocas et al.[60] reported that the deposition rate decreased at the positive substrate bias in the CCP-CVD process, which also indicates the presence of positively charged nanoparticles.

In general, nanoparticles generated in the gas phase of the plasma CVD process are known to be charged negatively because the mobility of electrons is much higher than that of ions in non-thermal plasmas. Therefore, both positively and negatively charged nanoparticles are expected to exist in the gas phase of the plasma CVD process of this study. However, Si nanoparticles are not deposited at the substrate biases of + 25 V and + 50 V, which indicates the non-existence below the grid. Therefore, negatively-charged Si nanoparticles, which are expected to exist in abundance in the plasma, appear to be blocked by the grid around which a sheath exists.[89] As shown in figure 21 (a), If the sheath is so thick that the sheath-free region disappears, negatively charged nanoparticles can be repelled by the sheath and may not be deposited on the substrate with the biases of + 25 V and + 50 V.

If the negatively charged nanoparticles are blocked by the sheath formed around the grid mesh, they may pass through the grid mesh if the mesh size is increased. In order to check this possibility, the mesh size was increased from 1 mm to 2 mm and the deposition behavior on the substrate was examined.

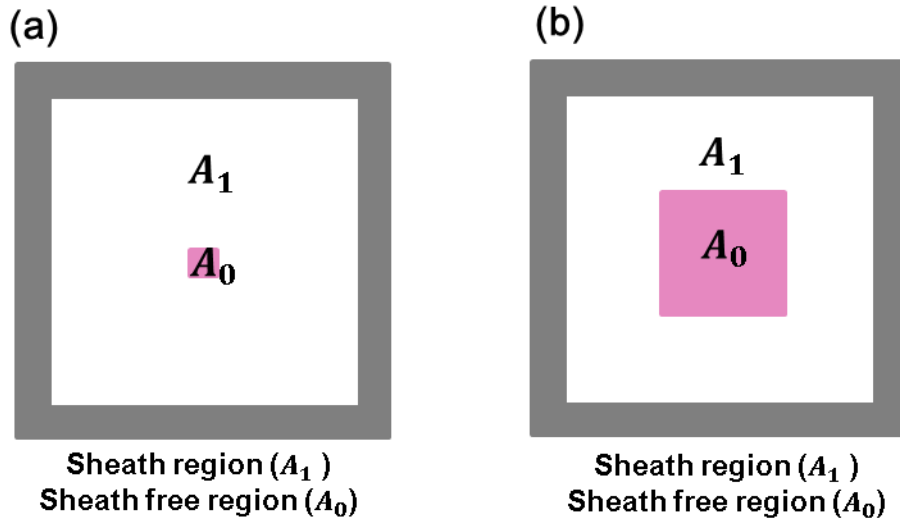


Figure 21. Microscopic diagrams for one cell of the grid (a) when the sheath is thick enough to overlap the hole of mesh, (b) when the sheath exist with the sheath-free region.[89]

Figure 22 shows the size distribution of the Si nanoparticles deposited on the substrate applied with bias from -50 V to + 50 V with the 2 mm meshes grid under the same condition as that of figure 20. As the substrate bias voltage was increased from - 50 V to + 50 V, the number density of Si nanoparticles continued to decrease and their size increased. The diameter range of Si nanoparticles of the highest frequency was 8 ~ 10, 14 ~ 16, 16 ~ 18, 18 ~ 20 and 40 ~ 45 nm at the substrate bias voltages of - 50, - 25, 0, + 25, and + 50 V, respectively. In contrast with the result with the grounded grid of 1 mm meshes, Si nanoparticles are deposited at the substrate biases of + 25 V and + 50 V. Therefore it appears that the increased mesh size generates the sheath-free region inside the mesh and negatively charged nanoparticles could pass through the mesh as shown in figure 21 (b).

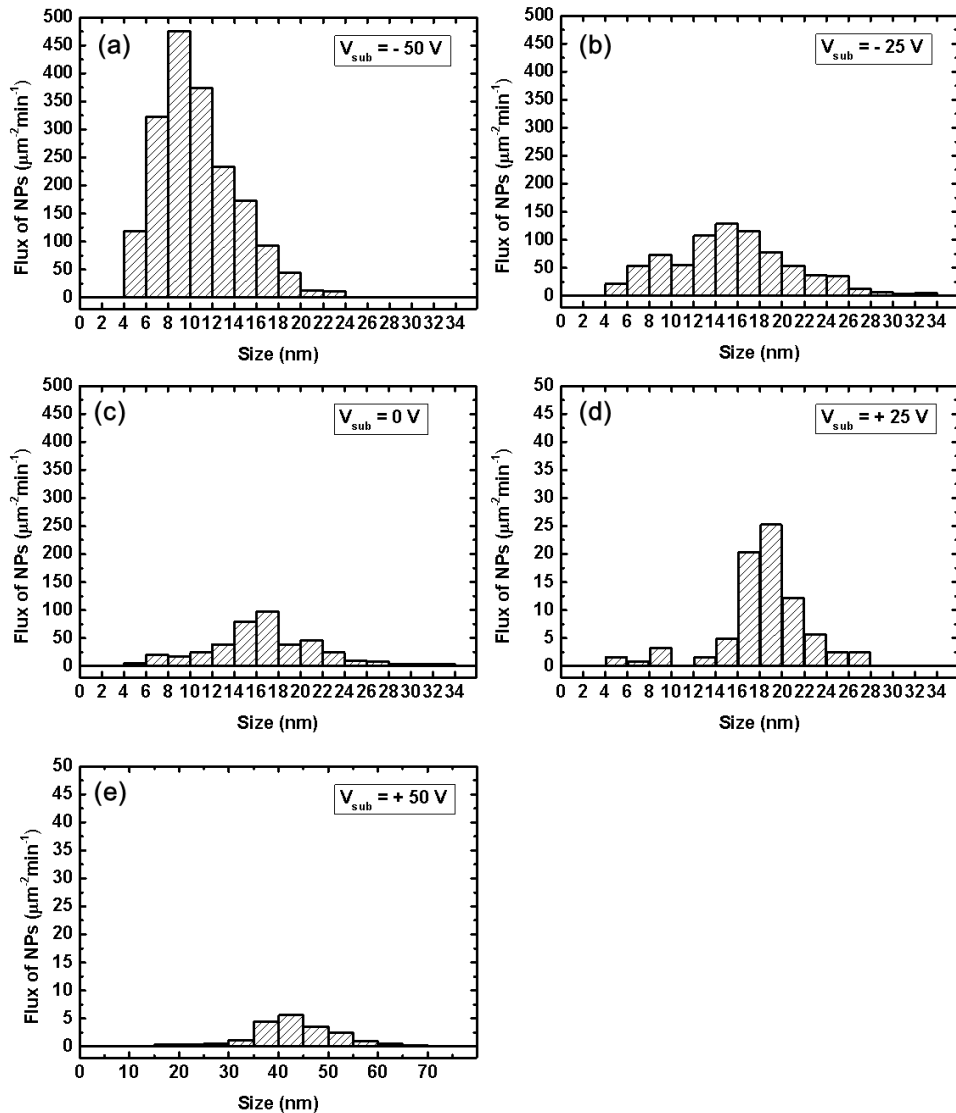


Figure 22. Size distributions and number density of Si nanoparticles for substrate bias of (a) -50, (b) -25, (c) 0, (d) + 25, and (e) + 50 V with grounded grid of 2 mm meshes at RF power of 1400 W.

To examine the possibility for the formation of the sheath-free region, plasma potentials were measured at the position above the grounded grid with various

substrate bias voltages as shown in figure 23. The plasma potential is affected by the substrate bias through the sheath-free region inside the mesh and increased with increasing substrate bias. At the substrate bias of + 50 V, the plasma potential was measured higher than the substrate bias potential at the position above the 2 mm mesh grid. However, the plasma potential was measured lower than the substrate bias potential at the position above the 1 mm mesh grid. This lower plasma potential than the substrate bias voltage for the substrate bias of + 50 V with the grounded grid of 1 mm meshes would be attributed to the decrease of the sheath-free region.

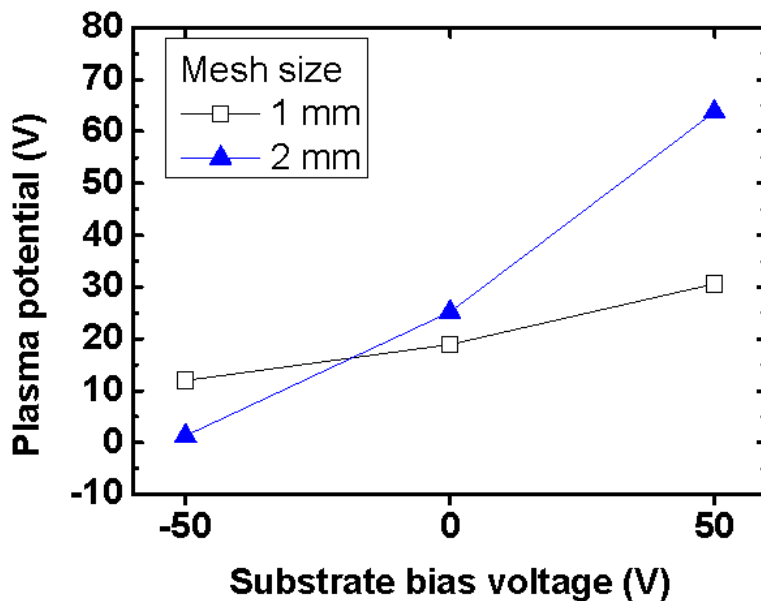


Figure 23. Plasma potentials measured with substrate bias of -50, 0, and + 50 V at RF power of 1400 W for grounded grids of 1 mm meshes (data of unfilled squares) and 2 mm meshes (data of filled triangles).

As shown in figure 22, Si nanoparticles deposited at the substrate bias of + 50

V with the 2 mm mesh grid are abruptly large in comparison with other Si nanoparticles deposited at other substrate biases. According to figure 23, the plasma potential was always higher than the substrate bias potential in the case of the 2 mm mesh grid. In this potential difference between the plasma and the substrate, positively charged nanoparticles would pass through the mesh mainly in spite of applying the substrate bias of + 50 V. The formation of the abruptly large nanoparticles cannot be explained by the agglomeration among positively charged nanoparticles because the aggregated positively charged nanoparticles have the size range of 10 ~ 11 nm as shown in Figure 20. On the other hand, it is reported that such large nanoparticles can be formed by rapid growth which is made possible when positively and negatively charged nanoparticles coexist. Therefore, it appears that the large nanoparticles deposited at the substrate bias of + 50 V with the 2 mm mesh grid were grown rapidly by the agglomeration of two oppositely-charged nanoparticles. Therefore, the effect of the substrate bias on the deposition behavior shown in Figures 3 and 4, indicates that the polarity and the size of nanoparticles passing through the grid can be controlled by the substrate bias and the mesh size.

Based on the understanding mentioned above, to control the length of sheath by another process parameter except the mesh size, effect of RF power on the deposition behavior of charged nanoparticles was investigated. Because it is well known that plasma density is decreased as the RF power decrease and the sheath length become thicker at lower plasma density.

Figure 24(a), (b), and (c) show the FE-SEM images for the Si nanoparticles

deposited on the substrate with the substrate bias of -50 , 0 , and $+50$ V under the pressure of 350 mTorr at RF power of 1000 W with the grounded grid of 2 mm. As shown in figure 24, the sizes of nanoparticles were not changed by applying the substrate bias. This result is understood that only positively charged nanoparticles are passed through the sheath-overlapped hole of mesh and deposited. On the other hand, the sizes of positively charged nanoparticles deposited at RF power of 1000 W is larger than that of nanoparticles deposited at RF power of 1400 W with grid of the 1 mm meshes. This is attributed that the plasma condition changed with decreasing RF power made the nanoparticles larger.

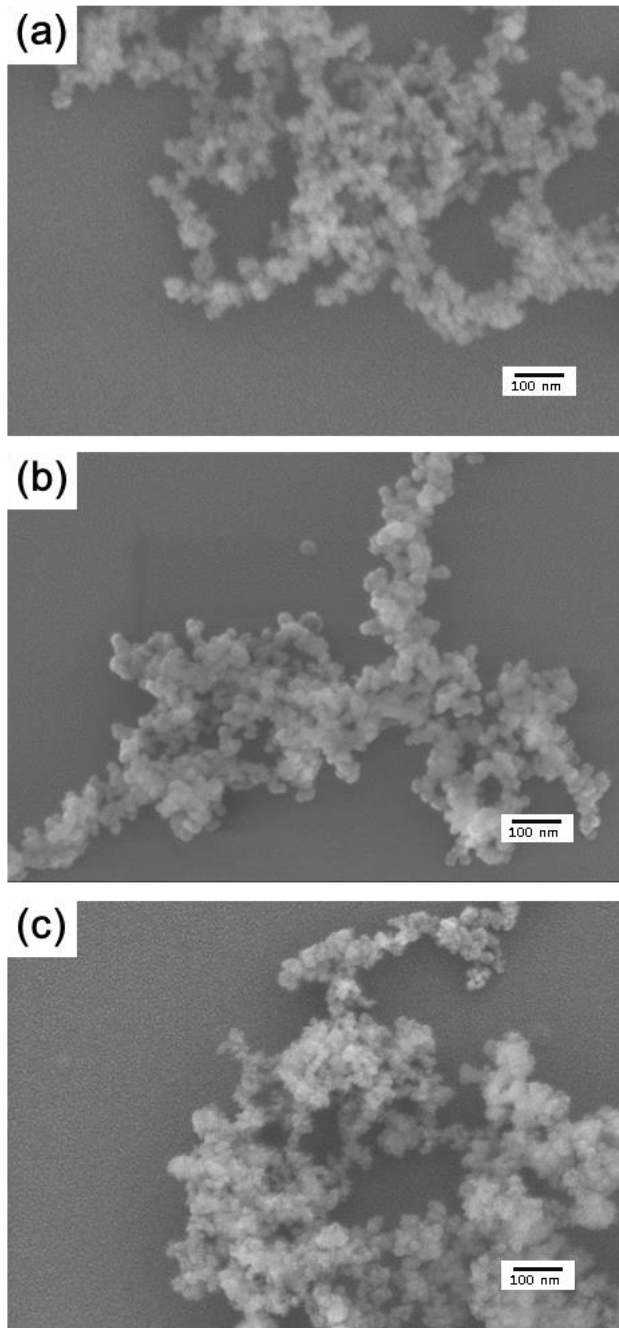


Figure 24. SEM images of Si Nanoparticles deposited by RF power of 1000 W at substrate bias of (a) -50, (b) 0, and (c) + 50 V with grounded grid of 2 mm.

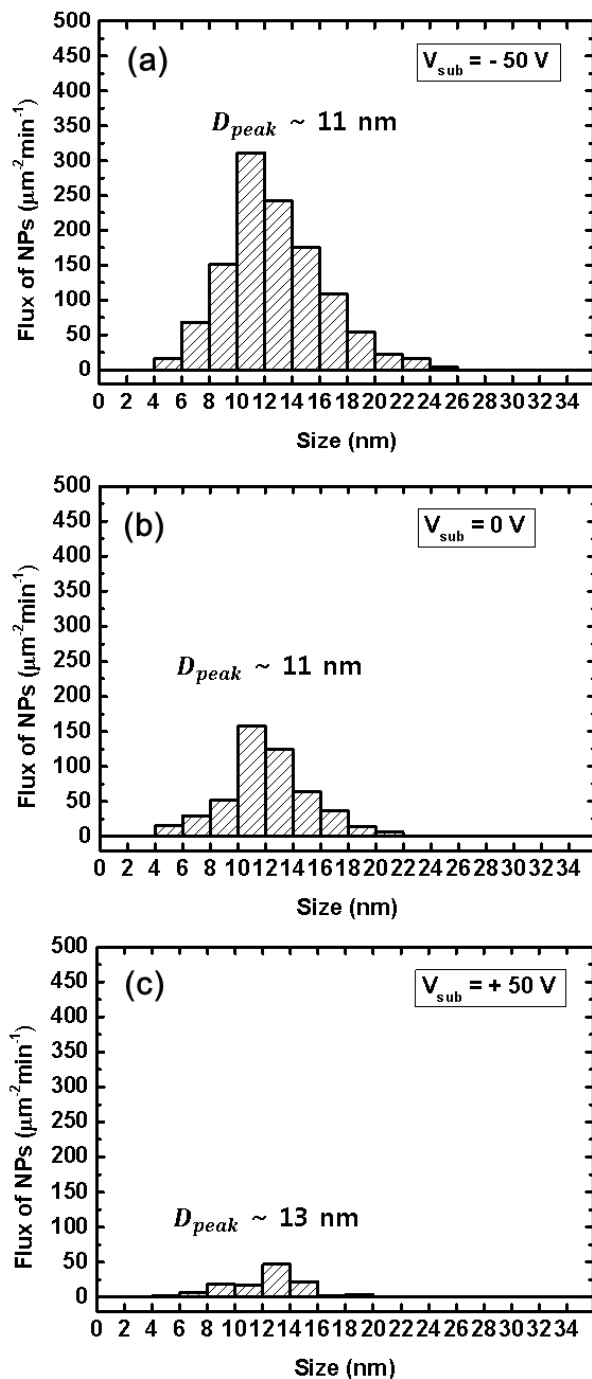


Figure 25. Size distributions and number density of Si nanoparticles for substrate bias of (a) -50, (b) 0, and (c) + 50 V with grounded grid of 2 mm meshes at RF power of 1700 W.

Figure 25(a), (b), and (c) show the size distributions and the number density of the Si nanoparticles deposited with the substrate bias of -50 , 0 , and $+50$ V under the pressure of 350 mTorr at the RF power of 1700 W with the grounded grid of 2 mm meshes. In the contrast with the result with RF power of 1400 W, the sizes of nanoparticles were little changed by applying the substrate bias. This result is understood that when the RF power is high considerably, the sheath is too thin as shown in figure 26(b) and the sheath-free region is so large that the grounded grid cannot confine the substrate from the plasma. As a result, the substrate bias cannot change the deposition behavior of charged nanoparticles.

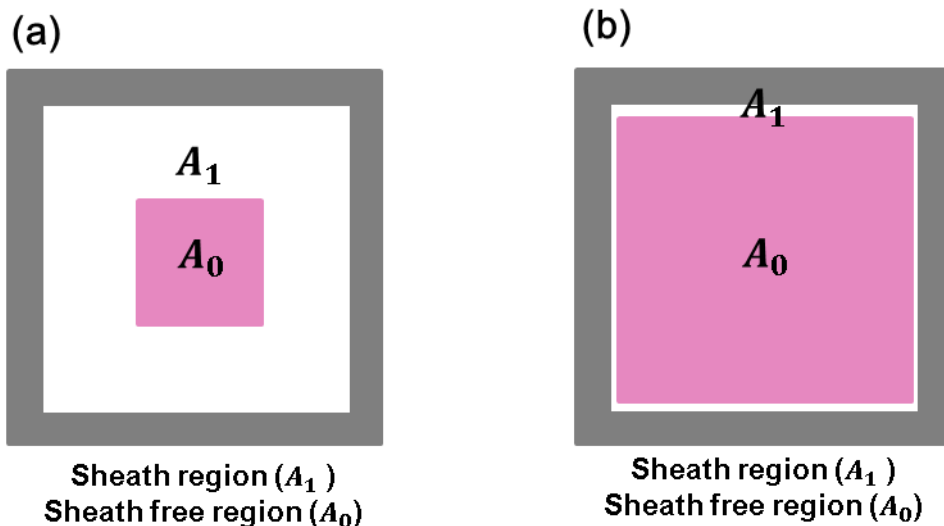


Figure 26. Microscopic diagrams for one cell of the grid (a) when the sheath exists with the sheath-free region, (b) when the sheath is too thin to confine the substrate from the plasma.

On the other hand, in the experiment with the 1mm mesh grid, RF power increased from 1400 W to 1700 W to open the closed sheath-overlapped region.

Figure 27 shows the size distribution and the number density of the Si nanoparticles deposited by RF power of 1700 W with the substrate bias of -50 , 0 , and $+50$ V under the pressure of 350 mTorr with the grounded grid of 1 mm meshes. As the substrate bias voltage was increased from -50 V to $+50$ V, the number density of Si nanoparticles was decreased continuously and nanoparticle size was increased. The diameter of Si nanoparticles of the highest frequency was 9, 9 or 13, and 19 nm at the substrate bias voltage of -50 , 0 , and $+50$ V, respectively. In contrast with the result at RF power of 1400 W with the grounded grid of 1 mm meshes, size of Si nanoparticles was increased more significantly as the substrate bias was increased from 0 V to $+50$ V. Therefore it is understood that the higher RF power generated the sheath-free region inside mesh and the substrate bias changed the deposition behavior of charged nanoparticles.

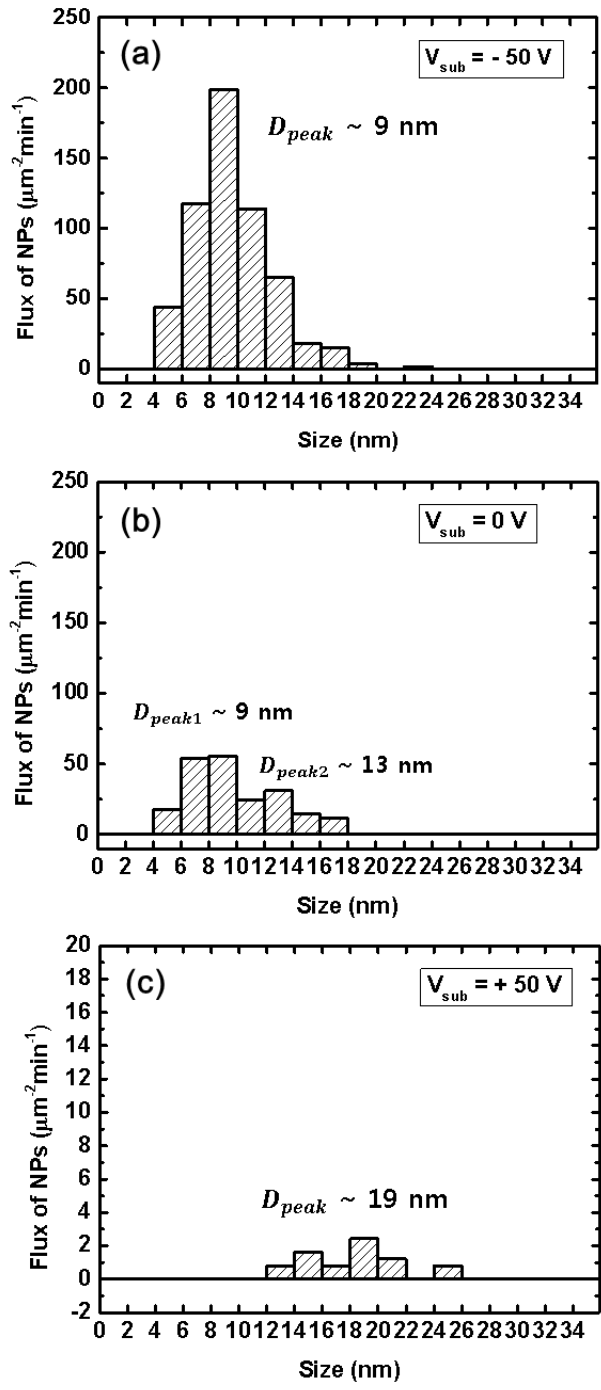


Figure 27. Size distributions and number density of Si nanoparticles for substrate bias of (a) -50, (b) 0, and (c) + 50 V with grounded grid of 1 mm meshes at RF

power of 1700 W.

4. CONCLUSION

By using the grounded grid, the film formation in the ICP-CVD process could be avoided and as a result crystalline nanoparticles could be produced on the substrate. Moreover, the applying the substrate bias, the amount and the size of crystalline nanoparticles could be controlled. From the result of the 1 mm mesh grid at RF power of 1400 W showing that the negative substrate bias increased the amount of nanoparticles, it is confirmed that positively charged crystalline nanoparticles are generated in the ICP-CVD process. And sizes of nanoparticles were controlled by applying the substrate bias in the condition where the area of sheath-free region exists enough to confine the plasma from the substrate.

Reference

- [1] P.B.a.G.H. Gilmer, *Crystal growth: An Introduction*, North-Holland, Amsterdam, 1973.
- [2] J.P.v.d. Eerden, *Handbook of crystal growth vol 1a Fundamentals 'Thermodynamics and Kinetics'*, North-Holland, Amsterdam, 1993.
- [3] H. Cölfen, M. Antonietti, *Mesocrystals and Nonclassical Crystallization*, John Wiley & Sons Ltd, West Sussex, England, 2008.
- [4] A. Glasner, J. Kenat, *J. Cryst. Growth*, 2 (1968) 119-127.
- [5] A. Glasner, S. Skurnik, *Isr. J. Chem.*, 6 (1968) 501-503.
- [6] A. Glasner, M. Tassa, *Isr. J. Chem.*, 12 (1974) 817-826.
- [7] A. Glasner, M. Tassa, *Isr. J. Chem.*, 12 (1974) 799-816.
- [8] G.D. Botsaris, R.C. Reid, *J. Chem. Phys.*, 47 (1967) 3689-3690.
- [9] I. Sunagawa, *Morphology of minerals*, in: I. Sunagawa (Ed.) *Morphology of Crystals*, Terra Sci, Tokyo, 1987, pp. 509-587.
- [10] I. Sunagawa, *J. Cryst. Growth*, 99 (1990) 1156-1161.
- [11] P. Roca i Cabarrocas, *J. Non-Cryst. Solids*, 266-269, Part 1 (2000) 31-37.
- [12] P. Roca i Cabarrocas, *Curr. Opin. Solid State Mater. Sci.*, 6 (2002) 439-444.
- [13] S.V. Vladimirov, K. Ostrikov, *Phys. Rep.*, 393 (2004) 175-380.
- [14] S. Nunomura, K. Koga, M. Shiratani, Y. Watanabe, Y. Morisada, N. Matsuki, S. Ikeda, *Jpn. J. Appl. Phys.*, 44 (2005) L1509.
- [15] N.M. Hwang, J.H. Hahn, D.Y. Yoon, *J. Cryst. Growth*, 162 (1996) 55-68.
- [16] N.M. Hwang, J.H. Hahn, D.Y. Yoon, *J. Cryst. Growth*, 160 (1996) 87-97.
- [17] N.M. Hwang, D.Y. Yoon, *J. Cryst. Growth*, 160 (1996) 98-103.
- [18] W.S. Cheong, N.M. Hwang, D.Y. Yoon, *J. Cryst. Growth*, 204 (1999) 52-61.
- [19] I.D. Jeon, C.J. Park, D.Y. Kim, N.M. Hwang, *J. Cryst. Growth*, 213 (2000) 79-82.
- [20] H.S. Ahn, H.M. Park, D.Y. Kim, N.M. Hwang, *J. Cryst. Growth*, 234 (2002) 399-403.
- [21] I.D. Jeon, M.C. Barnes, D.Y. Kim, N.M. Hwang, *J. Cryst. Growth*, 247 (2003) 623-630.
- [22] N.M. Hwang, D.Y. Kim, *Int. Mater. Rev.*, 49 (2004) 171-190.
- [23] J.I. Lee, N.M. Hwang, *Carbon*, 46 (2008) 1588-1592.
- [24] C.S. Kim, Y.B. Chung, W.K. Youn, N.M. Hwang, *Carbon*, 47 (2009) 2511.
- [25] C.S. Kim, Y.B. Chung, W.K. Youn, N.M. Hwang, *Aero. Sci. Tech.*, 43 (2009) 120.
- [26] C.S. Kim, I.J. Kwak, K.J. Choi, J.G. Park, N.M. Hwang, *J. Phys. Chem. C*, 114

- (2010) 3390-3395.
- [27] C.S. Kim, W.K. Youn, N.M. Hwang, *J. Appl. Phys.*, 108 (2010) 014313.
- [28] S.S. Lee, C.S. Kim, N.M. Hwang, *Aerosol Sci. Tech.*, 46 (2012) 1100-1108.
- [29] W.K. Youn, C.S. Kim, J.Y. Lee, S.S. Lee, N.M. Hwang, *J. Phys. Chem. C*, 116 (2012) 25157-25163.
- [30] N.M. Hwang, D.K. Lee, *J. Phys. D:Appl. Phys.*, 43 (2010) 483001.
- [31] S.S. Lee, M.S. Ko, C.S. Kim, N.M. Hwang, *J. Cryst. Growth*, 310 (2008) 3659-3662.
- [32] J.S. Hong, C.S. Kim, S.W. Yoo, S.H. Park, S.S. Lee, N.M. Hwang, H.M. Choi, D.B. Kim, T.S. Kim, *Curr. Appl Phys.*, 13 (Suppl. 2) (2013) S45-S49.
- [33] N.M. Hwang, *J. Cryst. Growth*, 204 (1999) 85-90.
- [34] W.A. Yarbrough, *J. Am. Ceram. Soc.*, 75 (1992).
- [35] K.E. Spear, *Journal of the American Ceramic Society*, 72 (1989) 171-191.
- [36] A. Badzian, N.M. Hwang, *Diamond: Low-Pressure Synthesis*, Reference Module in Materials Science and Materials Engineering, Elsevier 2016.
- [37] K. Choi, S.J.L. Kang, H.M. Jang, N.M. Hwang, *J Cryst Growth*, 172 (1997) 416-425.
- [38] I.-D. Jeon, C.J. Park, D.-Y. Kim, N.M. Hwang, *Journal of Crystal Growth*, 223 (2001) 6-14.
- [39] C.J.P. I. D. Jeon, D. Y. Kim, and N. M. Hwang, *J. Cryst. Growth*, 223 (2001) 6.
- [40] I.D. Jeon, C.J. Park, D.Y. Kim, N.M. Hwang, *Journal of Crystal Growth*, 223 (2001) 6-14.
- [41] L. Boufendi, A. Plain, J.P. Blondeau, A. Bouchoule, C. Laure, M. Toogood, *Appl. Phys. Lett.*, 60 (1992) 169.
- [42] A. Garscadden, B.N. Ganguly, P.D. Haaland, J. Williams, *Plasma Sources Sci T*, 3 (1994) 239-245.
- [43] A.A. Howling, L. Sansonnens, J.L. Dorier, C. Hollenstein, *J Phys D Appl Phys*, 26 (1993) 1003-1006.
- [44] E. Stoffels, W.W. Stoffels, G.M.W. Kroesen, F.J. deHoog, *J Vac Sci Technol A*, 14 (1996) 556-561.
- [45] S. Veprek, O. Ambacher, W. Rieger, K. Schopper, M.G.J. Veprek-Heijman, *Mater. Res. Soc. Symp. Proc.*, 1993, pp. 13-18.
- [46] H. Cölfen, M. Antonietti, *Angew. Chem. Int. Ed.*, 44 (2005) 5576-5591.
- [47] F.C. Meldrum, H. Cölfen, *Chem. Rev.*, 108 (2008) 4332-4432.

- [48] M. Niederberger, H. Cölfen, *Physical chemistry chemical physics : PCCP*, 8 (2006) 3271-3287.
- [49] E.R. Leite, C. Ribeiro, *Crystallization and Growth of Colloidal Nanocrystals*, 2012.
- [50] P.R.I. Cabarrocas, N. Chaâbane, A.V. Kharchenko, S. Tchakarov, *Plasma Physics and Controlled Fusion*, 46 (2004) B235-B243.
- [51] P. Roca i Cabarrocas, *Phys. Status Solidi C*, 1 (2004) 1115-1130.
- [52] i.C. Roca, P., *J. Non-Cryst. Solids*, 266–269, Part 1 (2000) 31-37.
- [53] K. Ostrikov, E. Neyts, M. Meyyappan, *Adv. Phys.*, 62 (2013) 113-224.
- [54] K. Ostrikov, *Rev. Mod. Phys.*, 77 (2005) 489.
- [55] S. Nunomura, M. Kita, K. Koga, M. Shiratani, Y. Watanabe, *Journal of Applied Physics*, 99 (2006) 083302.
- [56] Y. Watanabe, M. Shiratani, K. Koga, *Physica Scripta T*, 89 (2001) 29-32.
- [57] K. Koga, Y. Matsuoka, K. Tanaka, M. Shiratani, Y. Watanabe, *Applied Physics Letters*, 77 (2000) 196-198.
- [58] M. Shiratani, H. Kawasaki, T. Fukuzawa, T. Yoshioka, Y. Ueda, S. Singh, Y. Watanabe, *J. Appl. Phys.*, 79 (1996) 104-109.
- [59] U. Kortshagen, G. Mümken, *Physics Letters A*, 217 (1996) 126-132.
- [60] P. Roca i Cabarrocas, T. Nguyen-Tran, Y. Djeridane, A. Abramov, E. Johnson, G. Patriarche, *Journal of Physics D: Applied Physics*, 40 (2007) 2258-2266.
- [61] N. Chaâbane, V. Suendo, H. Vach, P. Roca i Cabarrocas, *Appl. Phys. Lett.*, 88 (2006) -.
- [62] K. Koga, K. Nishiyama, Y. Morita, G. Uchida, D. Yamashita, K. Kamataki, H. Seo, N. Itagaki, M. Shiratani, N. Ashikawa, S. Masuzaki, K. Nishimura, A. Sagara, *Journal of Nuclear Materials*, 438 (2013) S727-S730.
- [63] M.A. Lieberman, A.J. Lichtenberg, *Principles of plasma discharges and materials processing*; 2nd ed, Wiley2005.
- [64] S.H. Seo, J.H. In, H.Y. Chang, *J. Appl. Phys.*, 97 (2005).
- [65] X. Jiang, W.J. Zhang, C.P. Klages, *Phys. Rev. B*, 58 (1998) 7064-7075.
- [66] D. Xiao, K. Kazunori, Y. Daisuke, S. Hyunwoong, I. Naho, S. Masaharu, S. Yuichi, S. Makoto, H. Masaru, *Jpn. J. Appl. Phys.*, 55 (2016) 01AA11.
- [67] S.W. Yoo, J.S. Hong, S.S. Lee, C.S. Kim, T.S. Kim, N.M. Hwang, *Cryst. Growth Des.*, 14 (2014) 6239-6247.
- [68] S. Thompson, C.R. Perrey, C.B. Carter, T.J. Belich, J. Kakalios, U. Kortshagen,

Journal of Applied Physics, 97 (2005) 034310.

[69] P.R.i. Cabarrocas, N.-T. Th, Y. Djeridane, A. Abramov, E. Johnson, G. Patriarche, J Phys D Appl Phys, 40 (2007) 2258.

[70] S. Hamma, P. Roca i Cabarrocas, Journal of Applied Physics, 81 (1997) 7282-7288.

[71] N.J. Kramer, R.J. Anthony, M. Mamunuru, E.S. Aydil, U.R. Kortshagen, Journal of Physics D: Applied Physics, 47 (2014).

[72] T. Matsoukas, M. Russell, Journal of Applied Physics, 77 (1995) 4285-4292.

[73] F. Taccogna, European Physical Journal D, 68 (2014).

[74] F. Taccogna, S. Longo, M. Capitelli, Vacuum, 73 (2004) 89-92.

[75] M.J. Kushner, W.Z. Collison, M.J. Grapperhaus, J.P. Holland, M.S. Barnes, Journal of Applied Physics, 80 (1996) 1337-1344.

[76] S.J. You, H.Y. Chang, Physics of Plasmas, 13 (2006) 043503.

[77] A.P. Alivisatos, Science, 271 (1996) 933-937.

[78] V.L. Colvin, M.C. Schlamp, A.P. Alivisatos, Nature, 370 (1994) 354-357.

[79] S. Coe, W.-K. Woo, M. Bawendi, V. Bulovic, Nature, 420 (2002) 800-803.

[80] W.U. Huynh, J.J. Dittmer, A.P. Alivisatos, Science, 295 (2002) 2425-2427.

[81] K.S. Leschkies, R. Divakar, J. Basu, E. Enache-Pommer, J.E. Boercker, C.B. Carter, U.R. Kortshagen, D.J. Norris, E.S. Aydil, Nano Letters, 7 (2007) 1793-1798.

[82] L. Mangolini, E. Thimsen, U. Kortshagen, 2005 Proceedings of the 4th ASME Conference on Integrated Nanosystems: Design, Synthesis, and Applications, 2005, pp. 73-74.

[83] A. Bapat, M. Gatti, Y.P. Ding, S.A. Campbell, U. Kortshagen, Journal of Physics D: Applied Physics, 40 (2007) 2247-2257.

[84] C.Y. Jung, J.B. Koo, B.Y. Jang, J.S. Kim, J.S. Lee, S.S. Kim, M.H. Han, Thin Solid Films, 587 (2015) 142-149.

[85] T. Matsoukas, Journal of Colloid and Interface Science, 187 (1997) 474-483.

[86] U. Kortshagen, U. Bhandarkar, Physical Review E - Statistical Physics, Plasmas, Fluids, and Related Interdisciplinary Topics, 60 (1999) 887-898.

[87] A. Bouchoule, L. Boufendi, Plasma Sources Science and Technology, 2 (1993) 204-213.

[88] L. Mangolini, D. Jurbergs, E. Rogojina, U. Kortshagen, Journal of Luminescence, 121 (2006) 327-334.

[89] J.I. Hong, S.H. Seo, S.S. Kim, N.S. Yoon, C.S. Chang, H.Y. Chang, Physics of

Plasmas, 6 (1999) 1017-1028.

Independent Topics

Organo-Functionalization of Silicon Nanocrystals Synthesized by Inductively Coupled Plasma Chemical Vapor Deposition

Organo-Functionalization of Silicon Nanocrystals Synthesized by Inductively Coupled Plasma Chemical Vapor Deposition

Don-Sung Lee,[†] Dong-Hoe Choe,[†] Seung-Wan Yoo,[‡] Jung-Hyung Kim,[‡] and Hyun-Dam Jeong^{†,*}

[†]Department of Chemistry, Chonnam National University, Gwangju 500-757, Republic of Korea.

*E-mail: hdjeong@chonnam.ac.kr

[‡]Vacuum Center, Korea Research Institute of Standards and Science, Daejeon 305-340, Republic of Korea

Received November 24, 2015, Accepted February 18, 2016, Published online April 13, 2016

Octadecyl-terminated silicon nanocrystals (ODE-Si NCs) are obtained via a surface-initiated thermal hydrosilylation reaction on hydride-terminated Si NCs (H-Si NCs). Pristine Si NCs were synthesized at the gram scale by using inductively coupled plasma chemical vapor deposition (ICP-CVD). The H-Si NCs were produced through a chemical etching process with hydrofluoric acid (HF), ethanol (EtOH), and distilled water (d-H₂O). The results obtained from X-ray diffraction (XRD) and field emission scanning electron microscopy (FE-SEM) indicate that the synthesized Si NCs obtained via ICP-CVD have diamond cubic-structured silicon with a grain size of 10 nm and a densely packed Si NC array consisting of individual NCs. Organo-functionalized Si NCs, *i.e.*, ODE-Si NCs, are well soluble in organic solvent whereas pristine Si NCs synthesized through ICP-CVD are not. The surface chemistry of the ODE-Si NCs was confirmed via Fourier transform infrared spectroscopy (FT-IR), proton nuclear magnetic resonance spectroscopy (¹H-NMR), and field emission transmission electron microscopy (FE-TEM). Thereby, these newly synthesized and scalable organo-functionalized Si NCs are applicable as raw materials for practical use in devices by tuning the surface chemistry with various capping molecules.

Keywords: Silicon nanocrystal, Inductively coupled plasma chemical vapor deposition, Hydride-terminated silicon nanocrystal, Thermal hydrosilylation, Octadecyl-terminated silicon nanocrystal

Introduction

Over the years, the study of semiconductor nanocrystals (NCs) or quantum dots (QDs) has drawn a significant amount of attention due to their interesting fundamental physical properties, including their size-dependent characteristics that arise from the quantum confinement effect (QCE). The variation in their electronic structures according to their size allows the electrical and optical properties to be tuned,^{1–3} and among various semiconductor materials, silicon (Si) has been considered to be the most promising and suitable material due to its nontoxic and earth-abundant and also easy to integrate within well-established industrial silicon processes. In addition, recent studies on the synthesis of silicon nanocrystals (Si NCs) or silicon quantum dots (Si QDs) have made good use of Si in terms of tuning the particle size and surface capping molecule.^{4–8} These aforementioned advantages have prompted Si NCs or Si QDs to be applied in biophotonics,^{9,10} photoluminescent devices,^{11–13} lasers,¹⁴ sensors,¹⁵ and improved photovoltaic devices.^{16–18} Specifically, the anode materials in lithium ion batteries (LIB) have been used as an interesting application area for Si NCs due to their high lithium capacity and small size, ultimately reducing the mechanical stress that is induced by the high volume expansion during lithiation/delithiation.¹⁹

Various synthetic methods have been developed to facilitate the application of Si NCs or Si QDs, and these are typically divided into two categories: chemical or physical methods. In the chemical methodology, bare Si NCs or Si QDs are etched in order to generate hydride-terminated Si NCs (H-Si NCs). H-Si NCs are prone to oxidation and hence require surface functionalization or protection. Organo-functionalization can provide not only oxygen protection but also solution processability, and the solution process provides a superior adaptability to conventional applications, easy to synthesize, and the ability for mass production. Recently, our group reported on the surface functionalization of Si NCs or Si QDs by using a hydrosilylation reaction.^{20–26} Although this method provides unoxidized Si NCs with a narrow size distribution, it is challenging to mass produce high-quality crystals. For the physical methodology, several routes exist to synthesize Si NCs or Si QDs, including ion implantation,^{27–29} sputtering,^{30,31} electron beam reduction reaction (EBRR),³² and plasma-enhanced chemical vapor deposition (PECVD).^{29,33–36} These methods produce a high-quality product with a low defect density. However, they have critical drawbacks, including a high cost due to the harsh conditions needed, such as an ultrahigh vacuum, a relatively broad size distribution, and difficulties in functionalization.

Herein, we combine the chemical and physical methods to overcome the aforementioned difficulties of using conventional synthetic methods and in achieving mass production. Inductively coupled plasma (ICP) and thermal hydrosilylation were respectively adopted as the physical and chemical methodologies. ICP is related to PECVD and is of interest due to its low deposition temperature, fast deposition rate, and easy adaptability to various film deposition methods. The hydrosilylation reaction belongs to a one-pot synthesis where an alkene or alkyne reacts with a hydride-terminated Si (H-Si) surface in order to replace the Si-H bond with an Si-C covalent bond.³⁷ Photochemical, thermal, and catalytic methods have been developed in order to encourage the hydrosilylation reaction on porous silicon,³⁸⁻⁴⁰ surface of silicon nanoparticles,⁴¹⁻⁴³ and surface of single-crystal silicon.^{44,45} Among these, we have decided to use thermal hydrosilylation to functionalize H-Si NCs not only to avoid the lengthy separation and purification processes but also to increase the synthetic yield.

In this study, chemical etching and thermal hydrosilylation were employed to functionalize plasma-synthesized Si NCs (pristine Si NCs) with organic molecules. This newly developed hybrid synthetic method is demonstrated to be applicable in practice due to the production of a large amount of functionalized Si NCs as raw materials. For example, Si NCs can be functionalized with organic molecules to serve as a negative electrode material for LIB to be mass produced and compatible with the conventional non-aqueous polyvinylidene fluoride (PVDF) binder. In addition, the development of new material for practical use in devices requires a number of replicates. Hence our newly designed synthetic method is powerful to investigate new silicon nanomaterials compared to those reported in the literature. Namely this study presents a convenient and accessible way for silicon nanomaterial design. To the best of our knowledge, this is the first report that demonstrates the organo-functionalization of insoluble Si NCs synthesized by ICP-CVD by utilizing the advantages of both physical and chemical synthetic methodologies.

Experimental

Synthesis of Pristine Si NCs by ICP-CVD. Pristine Si NCs were synthesized in an ICP-CVD chamber with a mixture of hydrogen (H₂) and silane (SiH₄) gas as reactants. The plasma is sustained by applying a radiofrequency (RF) of 13.56 MHz at a power of 1500 W to a copper coil. A mixture of hydrogen-silane was used with the fraction of H₂ in the mixture gas at 0.90. To avoid agglomeration of the Si NCs generated in the gas phase and to control the microstructure of Si from the isolated Si NCs for the film, a grounded grid was inserted between the substrate and the plasma. A considerable amount of Si NCs were deposited on a silicon stainless steel substrate.

Organo-functionalization of Si NCs. The H-Si NCs were produced from 0.4 g of pristine Si NCs through an etching process using a 1:1:1 mixture (each 10 mL) of hydrofluoric acid (HF), ethanol (EtOH), and distilled water (d-H₂O). The mixture was stirred for 1 h to etch the partially oxidized components on the surface of the Si NCs, giving rise to the H-Si NCs. After completing the etching process, 30 mL of toluene was added. The unetched SiO₂ component was precipitated, and the H-Si NCs were dispersed in toluene (supernatant). The H-Si NCs were collected via centrifugation (15 000 rpm for 5 min), poured into reaction flask, and adding 10 mL of 1-octadecene (ODE). Then, the reaction mixture was degassed by conducting three evacuation/purge cycles with argon to eliminate water, and the samples were stirred for 12 h at 150 °C under Ar to produce octadecyl-terminated Si NCs (ODE-Si NCs). After cooling to room temperature, the product was washed three times via precipitation, with methanol as an antisolvent and toluene as a solvent. Finally, a bright brown resin was obtained after evaporating the toluene solvent via vacuum drying.

Characterization. The crystallinity of the Si NCs synthesized using ICP-CVD was characterized via X-ray diffraction (XRD) measurements. The XRD patterns were obtained on an X'Pert PRO Multiple Purpose X-ray diffractometer in the range of 2 θ = 10-90° with a Cu K α radiation source (λ = 1.5405 Å). The morphology of the Si NCs was measured via field emission scanning electron microscopy (FE-SEM). The SEM image was obtained using a JSM-7500F-JEOL instrument under a vacuum of approximately 1.0 \times 10⁻⁴ Torr with a power of 15 keV, and the sample was prepared on a grid with a carbon-tape and was then coated with platinum. The crystalline structure and chemical composition of the pristine Si NCs and the organo-functionalized Si NCs, *i.e.*, the ODE-Si NCs were investigated via field emission transmission electron microscopy (FE-TEM) and energy-dispersive X-ray spectroscopy (EDS) using a JEM-2100F electron microscope (JEOL, Akishima, Tokyo, Japan) at an accelerating voltage of 200 kV. For the TEM and EDS samples, a solution of 0.1 wt % of pristine Si NCs in ethanol and the ODE-Si NCs in hexane were drop-casted on a carbon-coated copper grid, and the solvents were evaporated under vacuum. The particle size was calculated by averaging the size of 150 particles from the TEM image through Gatan Microscopy Suite Digital Micrograph software (Gatan Inc. Ver. 2.11.1404.0, Pleasanton, CA, USA). Chemical bonding on the surface of the ODE-Si NCs was confirmed using Fourier transform infrared spectroscopy (FT-IR) and proton nuclear magnetic resonance spectroscopy (¹H-NMR). The FT-IR spectra were collected using a Spectrum 400-Perkin Elmer instrument, and the ¹H-NMR spectra were obtained using a Bruker 300.1 MHz NMR machine. The optical properties of the ODE-Si NCs were investigated via ultraviolet-visible (UV-vis) absorption and photoluminescence (PL) spectroscopies. UV-vis spectroscopy was

performed in the range from 200 to 1000 nm using a SCINCO S-3150 spectrophotometer (Gangnam-gu, Seoul, Korea). The PL spectra were measured using a TCSPC spectrofluorometer (Horiba Jobin Yvon Inc., Edison, NJ, USA) equipped with a 450-W Xenon lamp at an excitation wavelength of 250 nm and an R928P standard emission detector (240–850 nm).

Results and Discussion

Characterization of Pristine Si NCs Synthesized via ICP-CVD. An XRD analysis was used to investigate the crystallinity of the synthesized Si NCs. The XRD patterns of the Si NCs were measured in the range from 10 to 90°, and the results are shown in Figure 1. The XRD patterns reveal the formation of diamond cubic-structured Si NCs. Almost all precursors were completely decomposed, and no other complex products formed. The diffraction peaks and the relative intensities of the spectra coincide with the information in JCPDS card no. 27-1402.⁴⁶ The grain size of the Si crystallites was calculated using the Debye–Scherrer formula $D = 0.9\lambda/\beta\cos\theta$, where D is the grain size of the crystallite, λ is the wavelength of the incident X-rays ($=1.5405 \text{ \AA}$) that were used, β is the broadening of the diffraction line measured at half of its maximum intensity in radians, and θ is the angle of diffraction.⁴⁷ The grain size of the crystalline Si NCs was calculated to be about 10 nm.

The FE-SEM image shows the formation of a densely packed Si nanocrystal array that probably formed as a result of the high surface energy. The array consists of individual NCs of ~20 nm in diameter, as shown in the inset of

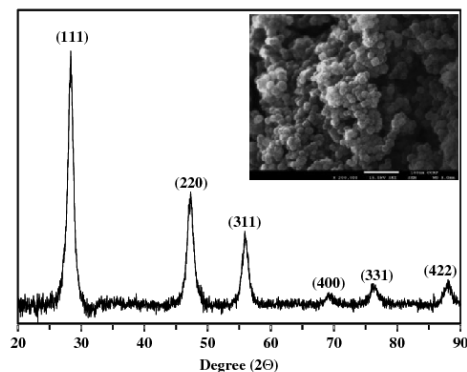


Figure 1. XRD and FE-SEM result for pristine Si NCs. XRD pattern indicating the formation of diamond cubic-structured Si NCs. The (111) main lattice plane was used to calculate the grain size. A FE-SEM image of the Si NC powders at a high magnification shows the formation of a densely packed Si NC array. The array consists of individual nanocrystals with a diameter of ~20 nm, as shown in the inset.

Figure 1. This discrepancy can be explained by the presence of a silicon oxide shell wrapping the crystalline core. We suggest that the oxide layer forms when the nanocrystals are exposed to air.

The size, size distribution, and crystalline structure of the pristine Si NCs are further investigated via TEM, as shown in Figure 2. The typical TEM images of the Si NCs show a number of overlapped Si NCs, and the high-resolution TEM image and size distribution histogram are shown in Figure 2(b) and (c). The average size (A_v) and standard deviation (SD) of the size distribution are 19.1 and 5.98 nm, respectively, indicating a broad size distribution. The lattice fringe with a d -spacing of 3.06 Å can be clearly seen, corresponding to the (111) plane of the diamond cubic-structured Si, as shown in Figure 2(d).^{22,48,49} The value of the d -spacing was calculated by averaging the distance of 10 grid intervals. The chemical composition of the Si NCs was investigated by EDS, as shown in Figure 2(e). Approximately 70% of the entire composition consists of Si, content, and carbon, oxygen, and copper contents possibly originate from impurities and the TEM copper grid. The full chemical composition of the Si NCs is summarized in Figure 2(f), and the TEM analysis can be used to conclude that the Si NCs synthesized by ICP-CVD were dominantly composed of Si and possessed a diamond cubic crystalline structure.

Organo-functionalization Mechanism on the Surface of Si NCs. The synthetic process and schematic illustration of the surface functionalization mechanism with ODE are shown in Scheme 1. In the case of a single-crystal silicon surface, Linford *et al.*⁴⁴ proposed that thermal hydrosilylation occurs on H–Si through a radical chain mechanism. Free energy activation barrier for abstraction of hydrogen from silicon by organic capping molecules such as an alkene or alkyne can be overcome by thermal excitation. The reaction is initiated by a silicon radical (dangling bond) originated either by a hydrogen abstraction from a surface Si–H group by the thermal excitation-generated radical. Once formed, the silicon radical may attack the C=C or C≡C bond of the alkene or alkyne very rapidly. A new covalent Si–C bond formed, and the radical migrates onto the secondary hydrocarbon atom. Subsequently, the hydrocarbon radical extracts a hydrogen atom from the adjacent Si–H bond at the H–Si surface, inducing a satisfied hydrocarbon chain and a new silyl radical on the Si surface. Because of the newly formed silyl radical, another alkene- or alkyne-terminated hydrocarbon molecule can react at this site. In this manner, the hydrosilylation reaction creates an Si–C bond on the Si surface with the organic molecule and leads to the final alkyl or alkenyl termination, *i.e.*, termination step. Ronald and Lopinski *et al.*^{45,50} reported strong experimental evidence to support the occurrence of this radical chain mechanism on the hydride-terminated single crystalline Si using scanning tunneling microscopy (STM) in an ultrahigh vacuum.

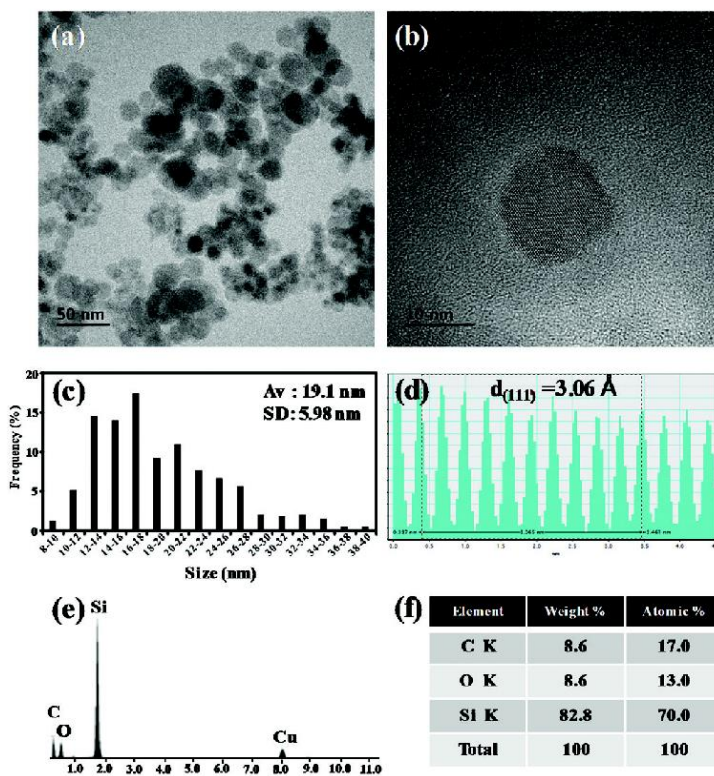
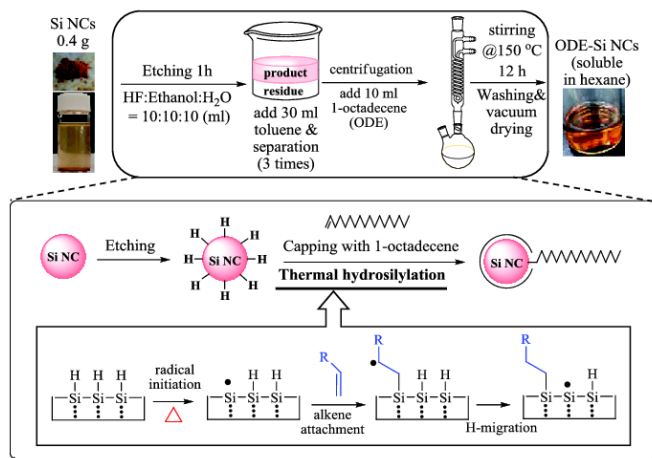


Figure 2. TEM results of pristine Si NCs. (a) Typical TEM image of the Si NCs showing a number of overlapped Si NCs. (b) High-resolution TEM image. (c) Size distribution of the Si NCs (Av is the average size of NC and SD denotes the standard deviation of the size distribution). (d) TEM histogram image showing a *d*-spacing value of 3.06 Å corresponding to the (111) plane of the diamond cubic-structured Si. (e) EDS spectrum of the Si NCs. Approximately 70% of the entire composition consists of Si content. (f) Chemical composition summary of the Si NCs.

Characterization of the ODE-Si NCs. The size distribution and the crystalline structure of the synthesized ODE-Si NCs were investigated via TEM, as shown in Figure 3. The typical TEM images of the ODE-Si NCs are shown in Figure 3(a), demonstrating a number of well-dispersed nanocrystalline phases. High-resolution TEM images and a size distribution histogram are shown in Figure 3(b) and (c). The average size and standard deviation of the size distribution are 12.7 and 4.28 nm, respectively, indicating that the ODE-Si NCs have a narrower size distribution than the pristine Si NCs. In addition, the average size of the crystal was reduced from 20 nm in pristine Si NCs to 12.7 nm in ODE-Si NCs. This discrepancy can be explained to be due to the removal of the silicon oxide layer on the surface of the pristine Si NCs through chemical etching. This

interpretation supports the aforementioned suggestion by XRD and FE-SEM that results from the pristine Si NCs as well. A lattice fringe with a *d*-spacing of 3.06 Å is shown in Figure 3(d) corresponding to the (111) plane of the diamond cubic-structured Si. The *d*-spacing value was calculated by averaging the distance of 10 grid intervals, and the chemical composition of the ODE-Si NCs was investigated via EDS, as shown in Figure 3(e). The carbon content was shown to have significantly increased, and the Si content dramatically decreased when compared to that in pristine Si NCs, as seen in Figure 2(e), probably because of the capping of the organic molecule (ODE) on the surface of the Si NCs. The full chemical composition of the Si NCs is summarized in Figure 3(f). The TEM analysis can be used to conclude that the ODE-Si NCs synthesized via thermal hydrosilylation were



Scheme 1. Synthetic illustration of the preparation of ODE-Si NCs. The H-Si NCs were produced via chemical etching, and the ODE-Si NCs were synthesized via thermal hydrosilylation. The radical chain hydrosilylation mechanism with a terminal alkene on a hydride-terminated Si NC surface is represented in a box.

mainly composed of carbon and Si, and the diamond cubic crystalline structure had been maintained.

Figure 4 shows a comparison of the FT-IR spectra for free ODE molecules (bottom) and the ODE-Si NCs (top). The free ODE molecule typically shows peaks from a terminal alkene group at 3078 cm^{-1} , 1640 cm^{-1} , and $908\text{--}987\text{ cm}^{-1}$, which corresponds to C=C-H stretching, C=C stretching, and C=C-H out-of-plane bending, respectively. The ODE-Si NCs show similar features when compared to those of free ODE molecules in the FT-IR spectra, indicating a similar chemistry on the surface of the Si NCs. The peaks at 2920 cm^{-1} , 2846 cm^{-1} , 1460 cm^{-1} , 1373 cm^{-1} , and 720 cm^{-1} were clearly observed and were attributed to the asymmetry, symmetry stretching of CH_2 , asymmetry bending of CH_2 , symmetry bending of CH_3 , and rocking of CH_2 , respectively. Additional low-intensity peaks for the ODE-Si NCs were detected at $1100\text{--}1000\text{ cm}^{-1}$ and were attributed to Si-O stretching, implying the presence of little oxidation on the ODE-Si NCs surface because of surface passivation by the ODE capping layer. In particular, the characteristic features of the vinyl groups had disappeared, as indicated by arrows, and the Si-H signal was not detected at 2100 cm^{-1} . We assume that the terminal vinyl group of the ODE had been almost entirely decomposed by the thermal hydrosilylation on the H-Si NCs. However, a detailed investigation was necessary for the hydrosilylation reaction because of the overlapping of CH_2 and Si-C scissoring in the range from $1450\text{ to }1460\text{ cm}^{-1}$.⁵¹

The surface chemical structure of the ODE-Si NCs was further confirmed via $^1\text{H-NMR}$ spectroscopy. Figure 5 shows a comparison of the $^1\text{H-NMR}$ spectra of the free

ODE molecules (bottom) before attachment on the Si NC surface and the ODE-Si NCs (top). In the $^1\text{H-NMR}$ spectrum of the free ODE molecule (bottom), the peaks were clearly assigned, as shown in the schematic inset: 5.81 (vinyl CH, b), 4.95 (vinyl CH_2 , a-a'), and 2.03 ppm (beside vinyl CH_2 , quartet, c). In addition, the signals from the protons of the methylene and methyl groups were found at 1.26 (CH_2 , d) and 0.88 ppm (CH_3 , triplet, e).

The integral ratio for a:b:c:d:e in the ODE free molecule is 1.0:1.0:2.2:28.5:3.3, which coincides well with the theoretical integral ratio of 1:1:2:28:3. In the $^1\text{H-NMR}$ spectrum of the ODE-Si NCs, the signals from the protons of the vinyl group almost entirely disappeared, as indicated by arrows, and two resonance protons (Si- CH_2 - (f) and - CH_3 (g)) are distinguishably found at 1.26 and 0.88 ppm.^{52,53} This is because capping the ODE on the surface of the Si NCs via thermal hydrosilylation results in the conversion of the vinyl group to the ethyl group in the ODE, which is consistent with the FT-IR results. The $^1\text{H-NMR}$ results further indicate that the ODE-Si NCs are covered by an octadecyl organic monolayer on the surface of the Si NCs, although the surface coverage cannot be determined, and such a surface structure of the ODE-Si NCs is illustrated in Figure 5 (top).

The optical properties of the ODE-Si NCs synthesized via thermal hydrosilylation were investigated via UV-vis absorption (dashed line) and PL (solid line) spectroscopy (Figure 6). The resulting ODE-Si NCs exhibit similar absorption characteristics as those reported in the literature,^{26,54,55} where the absorption spectrum has been found to consist of a featureless tail with an onset near $\sim 450\text{ nm}$ arising from the indirect band structure of the Si

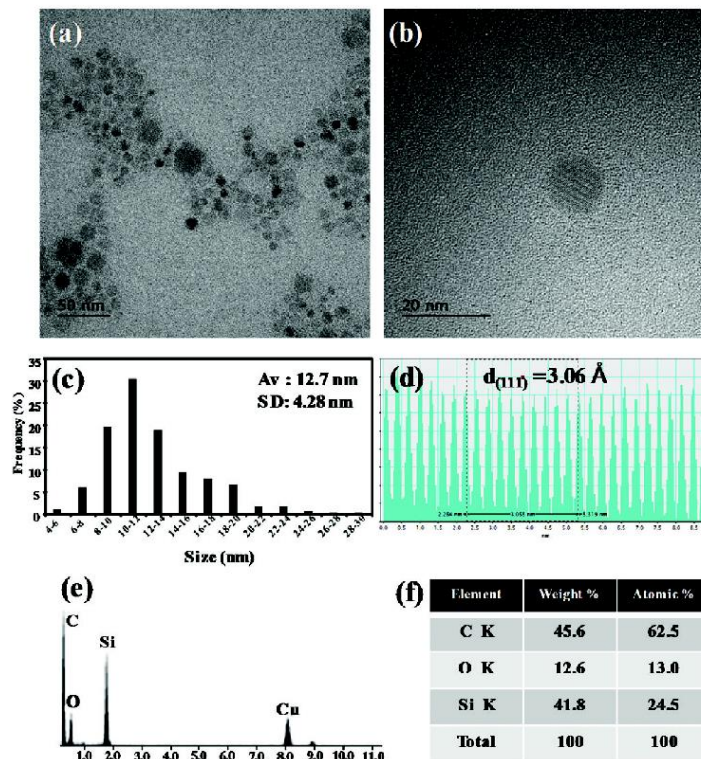


Figure 3. TEM images of the ODE-Si NCs. (a) Typical TEM image of ODE-Si NCs showing a number of well-dispersed nanocrystalline phases. (b) High-resolution TEM image. (c) Size distribution of ODE-Si NCs (A_v is the average size of NC and SD denotes the standard deviation of the size distribution). (d) TEM histogram image showing a d -spacing value of 3.06 Å corresponding to the (111) plane of diamond cubic-structured Si. (e) EDS spectrum of ODE-Si NCs. The carbon content increased significantly, and the Si content decreased dramatically when compared with that in pristine Si NCs. (f) Chemical composition summary of ODE-Si NCs.

NCs. In the PL spectrum, the ODE-Si NCs show a sharp peak at around 550 nm. Kim *et al.* reported that when the crystal size decreased from 6.1 to 2.6 nm, the PL peak shifted toward a lower wavelength from 1.46 (850) to 3.02 eV (410 nm). According to the effective mass approximation (EMA), the size of the ODE-Si NCs of 12 nm should show a PL peak near the IR, which is far from the results of the experiment. Hence such luminescence characteristics of the ODE-Si NCs are believed to have originated from the transition in the defect states,⁵⁶ not in the band-to-band domain. This is due to the fact that the band-to-band recombination should show QCE (inverse proportion of the band gap to the size). The energy gap, E , for the three dimensionally confined Si NCs can be expressed as E (eV) = $E_{\text{bulk}} + C/d^2$ according to EMA as well, where E_{bulk}

is the bulk crystal silicon band gap, d is the dot size, and C is the confinement parameter.⁵⁷

Conclusion

In this study, we have investigated a new class of easy and simple organo-functionalization methods for Si NCs via chemical etching and thermal hydrosilylation from pristine Si NCs synthesized via ICP-CVD. The presence of highly crystalline diamond cubic-structured pristine Si NCs of ca. 20 nm in size was confirmed in the XRD and FE-SEM analyses. The H-Si NCs formed through chemical etching and were then well capped by the ODE molecule in support of radical chain hydrosilylation mechanism, as confirmed via FT-IR, ¹H-NMR, and FE-TEM analyses. Visually,

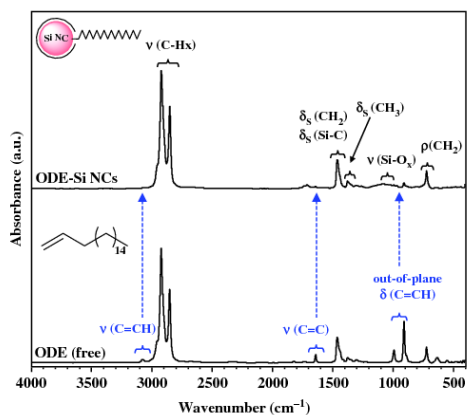


Figure 4. FT-IR spectra of the ODE free molecule (bottom) and the ODE-Si NCs (top). The stretching and bending vibration of a terminal vinyl group clearly disappeared, and oxidation peaks were rarely observed. The spectra were normalized to the intensity of aliphatic C–H stretching at 2846 cm^{-1} .

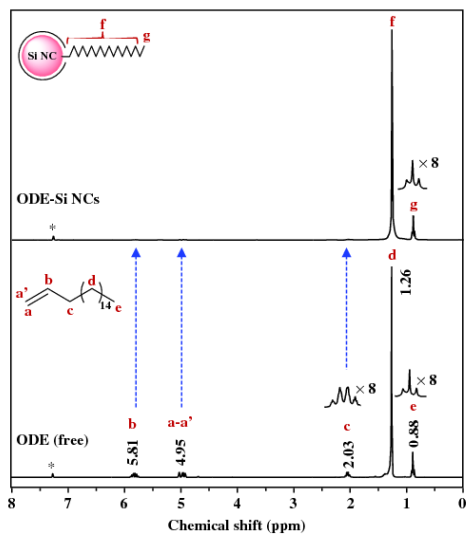


Figure 5. $^1\text{H-NMR}$ spectra of the ODE free molecule (bottom) and the ODE-Si NCs (top). $^*\text{CDCl}_3$ (NMR solvent, 7.26 ppm). The signals from the protons of the vinyl group (5.81, 4.95, 2.03 ppm) mostly disappeared, as indicated by arrows.

organo-functionalized Si NCs, *i.e.*, ODE-Si NCs, are well soluble and are optically transparent in organic solvent whereas pristine Si NCs are not, which means that the ODE

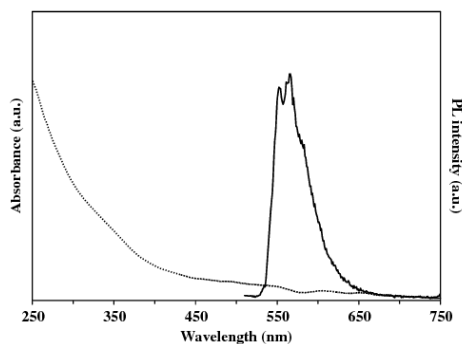


Figure 6. UV-visible absorption (dashed line) and PL (solid line) spectra of the ODE-Si NCs synthesized via chemical etching and thermal hydrosilylation of pristine Si NCs. In the absorption spectrum, the featureless tail (onset near ~ 450 nm) originates from an indirect band structure of the ODE-Si NCs. The PL peak at ~ 550 nm may originate from the few, small ODE-Si NCs with a size of about 3–4 nm.

molecule was well capped on the surface of the pristine Si NCs via thermal hydrosilylation. Furthermore, the surface protection or functionalization of Si NCs is the key point in practical devices due to the fact that the use of bare Si NCs would lead to an undesirable degradation in the devices originating from the oxidation problem. Hence, by utilizing the advantages of both the physical and chemical synthetic methodologies, mass-produced plasma synthesized Si NCs can be easily functionalized with organic molecules and can be applied in various important applications, such as in effective energy storage devices or as anode materials in LIB. Namely our newly designed synthetic method can be a good candidate to investigate practical silicon nanomaterials compared to those reported in the literature.

Acknowledgments. This research was supported by the Converging Research Center Program through the Ministry of Science, ICT and Future Planning, Korea (NRF-2014M3C1A8053709).

References

1. A. P. Alivisatos, *J. Phys. Chem.* **1996**, *100*, 13226.
2. W. W. Yu, J. C. Falkner, B. S. Shih, V. L. Colvin, *Chem. Mater.* **2004**, *16*, 3318.
3. M. V. Wolkin, J. Jome, P. M. Fauchet, *Phys. Rev. Lett.* **1999**, *82*, 197.
4. R. D. Tilley, J. H. Warner, K. Yamamoto, I. Matsui, H. Fujimori, *Chem. Commun.* **2005**, 1833–1835.
5. N. Shirahata, S. Furumi, Y. Sakka, *J. Cryst. Growth* **2009**, *311*, 634.
6. J. Wang, S. Sun, F. Peng, L. Cao, L. Sun, *Chem. Commun.* **2011**, *47*, 4941.

7. C. M. Hessel, E. J. Henderson, J. G. C. Veinot, *Chem. Mater.* **2006**, *18*, 6139.
8. M. Dasog, K. Bader, J. G. C. Veinot, *Chem. Mater.* **2015**, *27*, 1153.
9. J. Liu, F. Erogbogbo, K.-T. Yong, L. Ye, J. Liu, R. Hu, H. Chen, Y. Hu, Y. Yang, J. Yang, L. Roy, N. A. Karker, M. T. Swihart, P. N. Prasad, *ACS Nano* **2013**, *7*, 7303.
10. M. T. Swihart, *Nanotechnology in Biology and Medicine: Methods, Devices, and Applications* (Dinh T. V), CRC Press, Boca Raton, FL, **2007**, Chapter 4.
11. N. Lalic, J. Linnros, *J. Lumines.* **1999**, *80*, 263.
12. A. T. Fiory, N. M. Ravindra, *J. Electron. Mater.* **2003**, *32*, 1043.
13. R. K. Ligman, L. Mangolini, U. Kortshagen, S. A. Campbell, *Appl. Phys. Lett.* **2007**, *90*, 061116.
14. L. Pavesi, L. D. Negro, C. Mazzoleni, G. Franzò, F. Priolo, *Nature* **2000**, *408*, 440.
15. W.-J. Chiang, C.-Y. Chen, C.-J. Lin, Y.-C. King, A.-T. Cho, *Appl. Phys. Lett.* **2007**, *91*, 051120.
16. C. P. Rocai, N. Chaabane, A. V. Kharchenko, S. Tchakarov, *Plasma Phys. Controlled Fusion* **2004**, *46*, B235.
17. P. V. Kamat, *J. Phys. Chem. C* **2008**, *112*, 18737.
18. C.-Y. Liu, U. R. Kortshagen, *Nanoscale Res. Lett.* **2010**, *5*, 1253.
19. H. J. Kim, M. H. Seo, M.-H. Park, J. P. Cho, *Angew. Chem. Int. Ed.* **2010**, *49*, 2146.
20. X. D. Mai, H.-D. Jeong, *Bull. Korean Chem. Soc.* **2012**, *33*, 4185.
21. X. D. Mai, J.-K. Choi, H.-D. Jeong, *ACS Appl. Mater. Interfaces* **2013**, *5*, 2400.
22. X. D. Mai, D. T. Dao, S. H. Jeong, H.-D. Jeong, *Chem. Asian J.* **2013**, *8*, 653.
23. J.-K. Choi, X. D. Mai, H.-D. Jeong, *Mater. Chem. Phys.* **2014**, *148*, 463.
24. T.-H. Le, H.-D. Jeong, *Bull. Korean Chem. Soc.* **2014**, *12*, 3421.
25. T.-H. Le, H.-D. Jeong, *Bull. Korean Chem. Soc.* **2014**, *35*, 1523.
26. T.-H. Le, H.-D. Jeong, *Phys. Chem. Chem. Phys.* **2014**, *16*, 18821.
27. C. Bonafos, B. Colombeau, A. Altibelli, M. Carrada, G. B. Assayag, B. Garrido, M. López, A. Pérez-Podríguez, J. R. Morante, A. Claverie, *Nucl. Instrum. Methods Phys. Res., Sect. B* **2001**, *178*, 17.
28. Y. Q. Wang, R. Smirani, G. G. Ross, *J. Cryst. Growth* **2006**, *294*, 486.
29. M. Perálvarez, J. Barreto, J. Carreras, A. Morales, D. Navarro-Urrios, Y. Lebour, C. Domínguez, B. Garrido, *Nanotechnology* **2009**, *20*, 405201.
30. S. Charvet, R. Madelon, F. Gourbilleau, R. Rizk, *J. Appl. Phys.* **1999**, *85*, 4032.
31. S. Takeoka, *Phys. Rev. B* **2000**, *62*, 16820.
32. D.-S. Lee, H. S. Kang, Y.-S. Koh, B. C. Lee, H.-D. Jeong, *Bull. Korean Chem. Soc.* **2015**, *36*, 991.
33. F. Iacona, C. Bongiorno, C. Spinella, S. Boninelli, F. Priolo, *J. Appl. Phys.* **2004**, *95*, 3723.
34. T.-W. Kim, C.-H. Cho, B.-H. Kim, S.-J. Park, *Appl. Phys. Lett.* **2006**, *88*, 123102.
35. T.-T. Nguyen, C. Rocai, G. Patriarche, *Appl. Phys. Lett.* **2007**, *91*, 111501.
36. N. Daldosso, G. Das, S. Larcheri, G. Mariotto, G. Dalba, L. Pavesi, *J. Appl. Phys.* **2007**, *101*, 113510.
37. J. Holm, J. T. Roberts, *Langmuir* **2009**, *25*, 7050.
38. J. E. Bateman, R. D. Eagling, D. R. Worrall, B. R. Horrocks, A. Houlton, *Angew. Chem. Int. Ed.* **1998**, *37*, 2683.
39. R. Boukherroub, S. Morin, D. D. M. Wayner, D. J. Lockwood, *Phys. Status Solidi A* **2000**, *182*, 117.
40. J. M. Buriak, *Chem. Rev.* **2002**, *102*, 1271.
41. J. David, E. Rogojina, L. Mangolini, U. Kortshagen, *Appl. Phys. Lett.* **2006**, *88*, 233116.
42. J. Nelles, D. Sendor, A. Ebberts, F. M. Petrat, H. Wiggers, C. Schulz, U. Simon, *Colloid Polym. Sci.* **2007**, *285*, 729.
43. X. Zhang, D. Neiner, S. Wang, A. Y. Louie, S. M. Kauzlarich, *Nanotechnology* **2007**, *18*, 095601.
44. M. R. Linford, E. D. Chidsey Christopher, *J. Am. Chem. Soc.* **1993**, *115*, 12631.
45. R. L. Cicero, E. D. Chidsey Christopher, *Langmuir* **2002**, *18*, 305.
46. J. A. L. López, A. G. Román, E. G. Barojas, J. F. F. Gracia, J. M. Juárez, J. C. López, *Nanoscale Res. Lett.* **2014**, *9*, 1.
47. M. Caglar, Y. Caglar, S. Ilican, *J. Optoelectron. Adv. Mater.* **2006**, *8*, 1410.
48. M. Dasog, Z. Yang, G. C. V. Jonathan, *CrystEngComm* **2012**, *14*, 7576.
49. M. Sletnes, J. Maria, T. Grande, M. Lindgren, M.-A. Einarsrud, *Dalton Trans.* **2014**, *43*, 2127.
50. G. P. Lopinski, D. D. M. Wayner, R. A. Wolkow, *Nature* **2000**, *406*, 48.
51. C.-S. Yang, R. A. Bley, S. M. Kauzlarich, H. W. H. Lee, G. R. Delgado, *J. Am. Chem. Soc.* **1999**, *121*, 5191.
52. F. Hua, F. Erogbogbo, M. T. Swihart, E. Ruckenstein, *Langmuir* **2006**, *22*, 4363.
53. G. E. Zaikov, Y. B. Monakov, In *Trends in Molecular and High Molecular Science*, A. Jiménez Ed., Nova Science Press, Hauppauge, NY, **2005**, Chapter 20.
54. J. P. Wilcoxon, G. A. Samara, P. N. Provencio, *Phys. Rev. B* **1999**, *60*, 2704.
55. D. Tan, Z. Ma, B. Xu, Y. Dai, G. Ma, M. He, Z. Jin, J. Qiu, *Phys. Chem. Chem. Phys.* **2011**, *13*, 20255.
56. M. Dasog, Z. Yang, S. Regli, T. M. Atkins, A. Faramus, M. P. Singh, E. Muthuswamy, S. M. Kauzlarich, R. D. Tilley, J. G. C. Veinot, *ACS Nano* **2013**, *7*, 2676.
57. T.-Y. Kim, N.-M. Park, K.-H. Kim, G. Y. Sung, Y.-W. Ok, T.-Y. Seong, C.-J. Choi, *Appl. Phys. Lett.* **2004**, *85*, 5355.

국문 초록

유도결합플라즈마를 이용한 화학기상증착 공정 중에 생성되는 하전된 실리콘 나노 입자의 증착 거동에 미치는 기판 바이어스 효과를 비교전적 결정화 이론으로 접근하였다. 비교전적 결정화 이론이란 결정이 원자 또는 분자 단위에 의하여 생성되는 것이 아니라 나노입자에 의해 생성된다는 이론이다. 본 연구는 크게 두 가지 부분으로 나누어진다. 첫째는 유도결합플라즈마를 이용한 화학기상증착 공정 중 결정성 박막 생성시 하전된 실리콘 나노입자에 미치는 기판 바이어스 효과이며 둘째는 유도결합플라즈마를 이용한 화학기상증착 공정 중 결정성 나노입자 생성시 나노입자에 미치는 기판 바이어스 효과이다.

먼저, 결정성 박막 생성시, 기판 바이어스를 통하여 양으로 하전된 나노입자와 음으로 하전된 나노입자가 모두 플라즈마 조건에서 존재함이 확인되었다. 양으로 하전된 나노입자는 2.7 ~ 5.5 nm 크기였으며 음으로 하전된 나노입자는 6 ~ 13 nm 크기였다. 양으로 하전된 나노입자에 의한 박막보다는 음으로 하전된 나노입자에 의한 박막이 증착속도가 3 배가 빨랐으며 양으로 하전된 나노입자에 의한 박막은 일반적인 columnar 한 구조를 가졌다. 상온의 기판임에도 불구하고 결정성 박막이 증착된 것은 기상에서 생성된 결정성 실리콘 나노입자가 증착되었기 때문이다.

다음으로, 결정성 나노입자 생성시, 접지된 그리드와 기판 바이어스를 통하여 결정성 나노입자의 양과 크기를 변화시킬 수 있음을

확인했다. 1 mm 메쉬를 사용할 경우, 음의 기판바이어스를 가함에 따라 결정성 나노입자량이 증가한 반면 양의 기판 바이어스에서는 나노입자가 전혀 증착되지 않았다. 2 mm 메쉬를 사용할 경우 음의 기판 바이어스에서 양의 기판바이어스로 변화함에 따라 나노입자의 크기가 증가했다.

Keywords: silicon thin film, charged nanoparticles, nonclassical crystallization, ICP-CVD, substrate bias

Student Number: 2009-20620